Department of Physics and Astronomy
Heidelberg University

Bachelor Thesis in Physics
submitted by

Jonas Kleine

born in Olpe (Germany)

2024

Feasibility Study for the Reconstruction of very low p_T Pions, Kaons and Protons with ALICE in Run 3

This Bachelor Thesis has been carried out by Jonas Kleine at the
Physikalisches Institut in Heidelberg
under the supervision of
Prof. Dr. Klaus Reygers.

Abstract

This study investigates the feasibility of reconstructing very low p_T pions, kaons, and protons using the ALICE detector in Run 3. The lower momentum limits for particle identification in Run 2 were approximately 100 MeV/c for pions, 200 MeV/c for kaons, and 300 MeV/c for protons. Expanding this range is critical for studying phenomena such as Bose-Einstein condensates of pions and disoriented chiral condensates, both of which manifest at low momenta. The study employs a simplified standalone Geant4 simulation of ALICE's Inner Tracking System 2 (ITS2) and Time Projection Chamber (TPC) to explore the limitations of particle reconstruction in the low p_T region. In addition, PID using decay muons is explored as a potential method for particle identification. A machine learning (ML) model is also tested to improve reconstruction accuracy. Although the results indicate significant challenges at lower momenta –primarily due to energy loss and multiple scattering– PID with the conventional Bethe-Bloch method appears viable below the Run 2 limits. Moreover, machine learning PID methods shows promise in enhancing identification accuracy. The findings provide preliminary insights into the potential for low p_T particle reconstruction with ALICE, suggesting that further studies should follow.

Zusammenfassung

In dieser Studie wird untersucht, ob es möglich ist, Pionen, Kaonen und Protonen mit sehr niedrigem p_T mit dem ALICE-Detektor in Run 3 zu rekonstruieren. Die unteren Impulsgrenzen für die Teilchenidentifikation in Run 2 lagen bei etwa 100 MeV/c für Pionen, 200 MeV/c für Kaonen und 300 MeV/c für Protonen. Die Erweiterung dieses Bereichs ist entscheidend für die Untersuchung von Phänomenen wie Bose-Einstein-Kondensaten von Pionen und disoriented chiral condensates, die beide bei niedrigen Impulsen auftreten. Die Studie verwendet eine vereinfachte standalone Geant4-Simulation des Inner Tracking System 2 (ITS2) und der Time Projection Chamber (TPC) von ALICE, um die Grenzen der Teilchenrekonstruktion im niedrigen p_T-Bereich zu untersuchen. Darüber hinaus wird PID unter Verwendung von Zerfallsmuonen als mögliche Methode zur Teilchenidentifizierung untersucht. Ein machine learning Modell wird ebenfalls getestet, um die Rekonstruktionsgenauigkeit zu verbessern. Obwohl die Rekonstruktion auf Probleme bei niedrigeren Impulsen stößt - hauptsächlich aufgrund von Energieverlust und Mehrfachstreuung - scheint PID mit der konventionellen Bethe-Bloch-Methode unterhalb der Run-2-Grenzen praktikabel. Darüber hinaus erweisen sich PID-Methoden mit maschinellem Lernen als vielversprechend für die Verbesserung der Identifizierungsgenauigkeit. Die Ergebnisse geben erste Einblicke in das Potenzial für die Rekonstruktion von Teilchen mit niedrigem p_T mit ALICE in Run 3 und legen nahe, dass weitere Studien folgen sollten.

Table of contents

1 Introduction

The search for exotic events has always been a part of the heavy-ions physics program of the ALICE detector at CERN. Expanding the range of measurable particles within the experiment is critical to advancing this research. In Run 2, the lower limits for pions, kaons and protons are at approximately 100, 200 and 300 MeV/c [1]. Investigating low-momentum charged particles is crucial for testing various theories, such as the disoriented chiral condensate (DCC) theory and the formation of Bose-Einstein condensates of pions, both of which manifest at low momenta [2] [3]. Therefore, developing reliable methods to measure and classify low-momentum pions and other particles is a logical step. A similar idea has already been pursued at the RHIC collider, where the differential energy loss measurement with silicon detectors was used to classify the particles [4]. As the ITS2, the innermost tracking device of ALICE in Run 3, is not designed to properly measure the energy loss this way, another method has to be found and tested. The primary goal of this thesis is to conduct a feasibility study on the physical limitations of particle reconstruction and classification using the conventional PID methods. To achieve this, a simulation of the innermost detectors of ALICE was performed using a simplified standalone Geant4 setup. Additionally, the data will be used to train a machine learning model, to investigate whether it yields more accurate results than the conventional methods. For particles that do not have energy loss measurements, the idea is to measure the momentum of the primary particle with the ITS2 and then proceed to use the decay products for the full identification. The simplified Geant4 simulation serves as a preliminary exploration to determine the potential and limitations of this approach.

1.1 PHOBOS Experiment

In 2004 a similar study was made at the PHOBOS experiment at the relativistic heavy ion collider (RHIC) at the Brookhaven National Laboratory, to enhance the lower momentum limit PID of protons, kaons and pions [4]. The PID relied on precise measurements of the energy deposition in the PHOBOS detector, specifically using its silicon layers to identify low transverse momentum particles. The six innermost layers, that are located near the beam pipe, were used in a nearly field free setup to measure the energy deposition from charged particles. There is minimal material between the layers, and they are positioned very close to the collision point, allowing for an accurate detection and PID of low p_T particles.
The PID was limited to particles that stopped in the fifth silicon layer of the detector, by differentiating particles based on their energy deposition, as the low momentum particles lose substantially more energy than the higher energetic ones.
To estimate the particle mass, a mass parameter M_p based on the energy loss in the first four layers was constructed. As the particles decayed in the fifth layer, there were additional contributions from the particle's annihilation and or decay products in the energy deposition. Therefore, the energy deposition in this layer was estimated and later combined with the other

energy measurements to refine the particle mass calculation.
After some additional cuts and background subtraction techniques, to lower the contamination with secondary and misidentified particles, the study found an accurate determination of the particle's momentum and PID in the range of 140–210 MeV/c for protons, 90–130 MeV/c for kaons and 30–50 MeV/c for pions, which can be seen in Fig. 1 [4].
As for the ALICE in Run 3, there is no energy measurement done within the innermost detector unit [5], the ITS2, which stops us from pursuing the same approach.

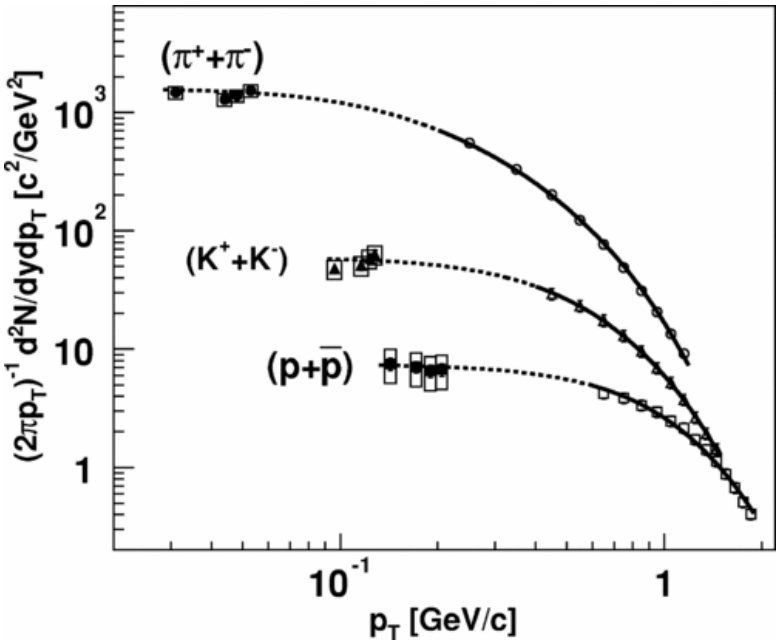

Figure 1: Invariant yields as a function of p_T at the PHOBOS detector [4]

.

1.2 Standard Model

Particle physics is the most fundamental theory, which deals with the interaction of the elementary particles in regard to the three fundamental forces, the electromagnetic-, weak- and strong force. The elementary particles are divided into fermions, which have half integer spin and bosons with integer spins. The bosonic particles function as a mediator of the forces between the fermions. The fermions can further be separated into leptons and quarks. The key difference here is that quarks interact with the strong force, whereas leptons do not. Lastly, these quarks and leptons can all be divided into three families. Our current knowledge is reflected in the standard model, which successfully describes the current experimental data [6].

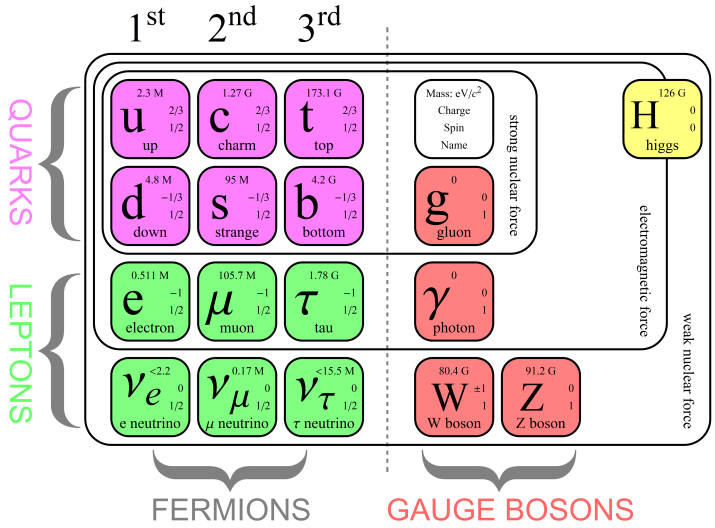

Figure 2: Elementary particles in the Standard Model [7]

1.3 QCD

Hadrons are bound states of quarks, which are held together by the strong interaction mediated by so-called gluons. These gluons couple to the color charge of the quarks, which is described by Quantum Chromodynamics (QCD). As a whole there are three colors, red, green and blue and their respective anti-colors, and 8 gluons. Other than in QED, the theory of the electromagnetic interaction, the exchange particle carries the charge of the interaction and are composed of one color and one anti-color.
Hadrons are divided into two main categories, baryons (such as protons and neutrons) which consist of three quarks, and mesons (such as pions and kaons), which are made of one quark and one antiquark.

1.4 Particles

1.4.1 Proton

The proton is a stable baryon with a composition of two u and one d quark and weighs around 938.27 MeV/c^2. The antiproton being stable, too, has analogously a composition of two anti u quarks and an anti d quark. Still, the antiproton will annihilate with a proton in most cases into five pions, more specifically $p + \overline{p} \rightarrow \pi^+ + \pi^- + \pi^0 + \pi^+ + \pi^-$ [8].

1.4.2 Kaon

The kaon is the lightest strange Meson with a mass of 493.68 MeV/c^2. The K^- consists of an $\bar{u}$ and a s quark. Respectively, the K^+ consists of an u and a $\bar{s}$ quark and has a mean lifetime of $1.23 \cdot 10^{-8}$ s. Its decay channels are given in Tab. 1 [8].

Decay Channel	Decay Products	Branching ratio
I.	$\mu^+\nu_\mu$	63.56%
II.	$\pi^+\pi^0$	20.67%
III.	$\pi^+\pi^+\pi^-$	5.58%
IV.	$\pi^0 e^+\nu_e$	5.07%
V.	$\pi^0\mu^+\nu_e$	3.35%

Table 1: 5 most common decay channels of the K^+ [8]

1.4.3 Pion

Pions are the lightest mesons and therefore also the lightest hadrons with a mass of 139.57 MeV/c^2 (charged pions) and 134.98 MeV/c^2 (neutral pion), and consist of a quark antiquark combination of the u and the d quark. The charged pions, being of special significance for this thesis, consist of an u quark and an anti d quark (π^+) or an anti u and a d quark (π^-). Other than for kaons with a range of possible decay channels, charged pions nearly exclusively decay into a muon and a muon neutrino, with a chance of 99.98 % and a mean lifetime of $2.6 \cdot 10^{-8}$ s [8].

1.5 Energy loss of charged particles in matter

When a charged particle transverses through matter at a velocity of $\beta\gamma \geq 0.1$, it ionizes the particles on its path. Therefore, the charged particles lose an amount of energy *dE*. The first relativistic and quantum mechanical theory was developed by Hans Bethe and later extended by Felix Bloch [9, 10]. The average differential energy loss is described by the theory of Bethe and Bloch and reads

$$-\left[\frac{dE}{dx}\right] = \frac{4\pi N e^4}{m_e^2}\frac{z^2}{\beta^2}\left[\ln\left(\frac{2m_e c^2 E_{max}\beta^2\gamma^2}{I^2}\right) - \beta^2 - \frac{\delta(\beta)}{2}\right] \tag{1}$$

where N is the electron density, e the elementary charge, z the charge of the particle, m_e the electron mass, c the speed of light and I the average effective ionization energy of the atomic electrons. At relativistic velocities, polarization effects of the surrounding electrons arise, which restrict the electric field of the particle. Therefore, Fermi extended the formula by introducing the density term $\delta(\beta)$ [11]. In Fig. 3, the differential energy loss of a muon in copper is plotted as a function against the velocity $\beta\gamma$.

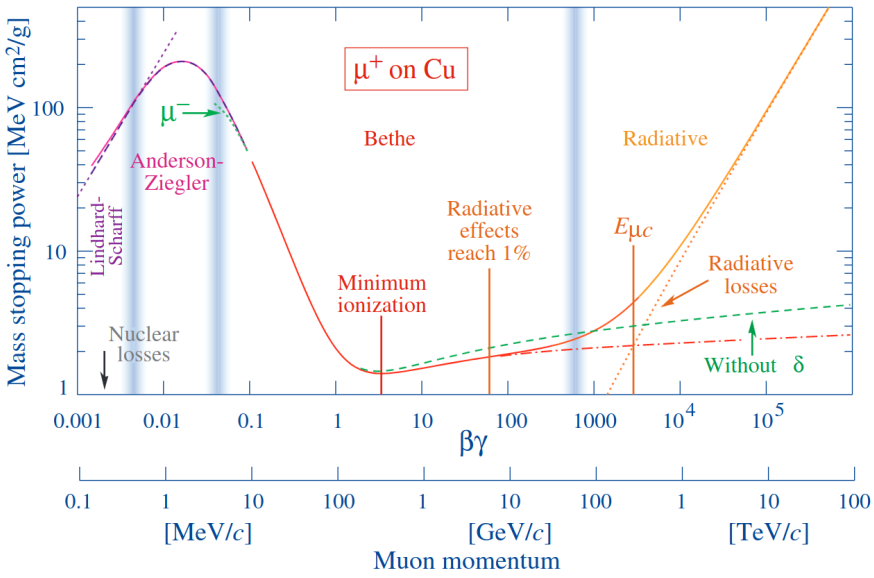

Figure 3: Average specific energy loss of muons in copper as a function of the velocity $\beta\gamma$ [12]

It is split into different regimes, that are described by different theories. For the scope of this thesis, the analysed momentum region lies entirely within the region described by the Bethe-Bloch formula (Eq. 1). Therefore, the other energy regions will not be discussed any further. The Bethe-Bloch energy loss decreases with increasing velocity at a rate $\propto \beta^{-2}$ to a minimum at around $\beta\gamma \approx 3$. The particles at this minimum are called "Minimum Ionizing Particles" (MIPs). After the minimum ionization, the energy loss has a logarithmic rise due to a higher transversal electric field as the velocity becomes relativistic. Moreover, the maximum energy deposition gets higher, however, this is limited by the density term of Fermi.

1.6 Multiple Scattering

Charged particles travelling through a medium undergo numerous small-angle deflections due to successive interactions with the nuclei and electrons of the material. These repeated deflections accumulate over the particle's trajectory, leading to a net change in its direction, which causes issues in the reconstruction of a particle's momentum.

In order to illustrate the effect of multiple scattering, it is useful to employ a geometrical representation, which can be seen in Fig. 4. One can see how the particle undergoes a series of directional changes, resulting in an overall deflection angle θ_{plane} and an offset y_{plane} with respect to the particle's original trajectory. It should be noted that, within the context of this description, the principle of momentum conservation has been assumed, and potential energy losses have been neglected [13].

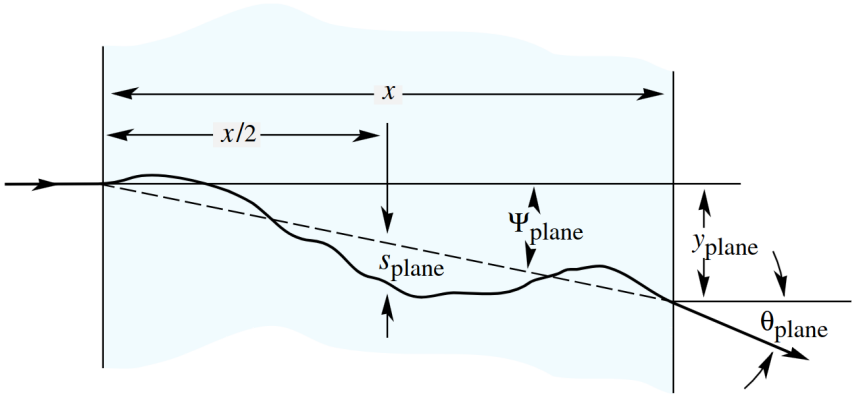

Figure 4: Sketch of multiple Coulomb scattering with describing quantities [13]

The scattering angle distribution follows a Gaussian distribution with a mean of $\overline{\theta} = 0$ and a standard deviation θ_0 given by the so-called Highland formula [14]:

$$\theta_0 = \frac{13.6 \text{ MeV}}{\beta cp} z \sqrt{\frac{X}{X_0}} \left[1 + 0.0038 \ln \left(\frac{X}{X_0} \right) \right] \tag{2}$$

with the charge number z, βc the velocity and p the momentum of the particle, the thickness of the material X and its radiation length X_0.
This scattering angle eventually leads to a momentum reconstruction error, following:

$$\frac{\sigma_p}{p} = 52.3 \times 10^{-3} \text{ GeV}/c \frac{\sqrt{X/X_0}}{\beta X B} \tag{3}$$

with the magnetic field strength B.

1.7 Least Squares Fitting and χ^2-Test

For the track reconstruction, various functions like a circle and helix function, later defined in Chapter 7, need to be fitted on the simulated tracks. Least squares fitting is a method used to determine the best-fitting curve or line to a set of data points by minimizing the sum of the squares of the differences between the observed values and the values predicted by the model [15].
Given a set of n data points (x_i, y_i) and their uncertainty σ_i, the goal is to fit a function $y = f(x)$ by minimizing the residuals, defined as the differences between the observed data y_i and the model predictions $f(x_i)$. The residual for the i-th data point is:

$$r_i = y_i - f(x_i) \tag{4}$$

The sum of squared residuals S is given by:

$$S = \sum_{i=1}^{n} (y_i - f(x_i))^2 \tag{5}$$

The best-fit parameters of the function $f(x)$ are determined by minimizing S.

The Chi-Squared test is a statistical method used to assess how well a theoretical model fits observed data [16]. For a set of data (x_i, y_i), the Chi-Squared statistic χ^2 is defined as:

$$\chi^2 = \sum_{i=1}^{n} \frac{(y_i - f(x_i))^2}{y_i} \tag{6}$$

A lower value of χ^2 indicates a better fit between the model and the data. The reduced chi-squared statistic χ^2_{red} is often used to normalize for the degrees of freedom $N_{\text{dof}} = n - p$, where p is the number of parameters in the model:

$$\chi^2_{\text{red}} = \frac{\chi^2}{N_{\text{dof}}} \tag{7}$$

A χ^2_{red} value close to 1 suggests that the model provides a good fit to the data, while values significantly greater or less than 1 indicate overfitting or underfitting, respectively.

1.8 Work structure

Before proceeding with the analysis, a simulation setup must be established to generate data in previously unexplored momentum regions. This step is essential to ensure that the results are meaningful and has some predictive power in regard to the real ALICE experiment. Although a simplified setup will be used to reduce complexity and computational time, allowing for more extensive exploration and analysis, the results will be compared to real data from near the uncharted regions to assess their reliability.

After setting up the simulation, the initial phase of the analysis will involve using the simulation data to reconstruct key particle properties, such as momentum and charge, and investigating any reconstruction errors that arise.

Subsequently, the reconstructed properties will be used to evaluate the performance of existing particle identification (PID) methods, such as the PID via the Bethe-Bloch formula, and to explore the benefits of supplementing these methods with a machine learning framework. This evaluation will determine whether conventional PID methods, proven effective in higher momentum regions, are also reliable in lower momentum regions.

Additionally, a new PID method specifically for kaons and pions will be tested.

The results of this analysis will provide guidance on the feasibility of pursuing studies in low momentum regions at lower magnetic fields. This study should be viewed as an exploratory

feasibility assessment rather than as definitive results, offering initial insights into potential limitations and challenges in this low momentum region.

2 ALICE

ALICE (A Large Ion Collider Experiment) is a detector unit of the LHC at the CERN, which is specialized on heavy ion detection with a focus on QCD interactions. This allows the study of hadrons, electrons, muons, and photons produced in the collision to develop a classification in the low momentum regime [17].

2.1 ALICE 2

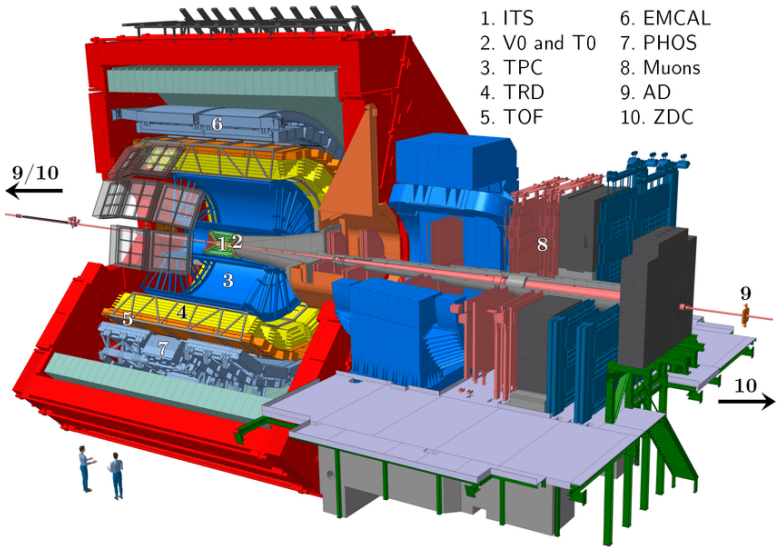

Figure 5: ALICE 2 detector layout [18]

ALICE 2 is the currently running detector with an overall dimension of 16x16x26 m^3 and an approximated weight of 10000t. The ALICE detector made up from a central barrel part, which is used to measure hadrons, electrons, photons and muons. The barrel is composed of individual detector units which from the innermost detector beginning is the upgraded Inner Tracking System 2 (ITS2), which contains seven concentric layers of Monolithic Active Pixel Sensors (MAPS) [5]. Adjacent to the ITS is the TPC, the cylindrical Time Projection Chamber, followed Transition Radiation Detector (TRD). Afterwards, the ALICE detector has Time-of-Flight (TOF) with its three particle identification arrays and Ring Imaging Cherenkov (HMPID) detectors. The final layers of the central barrel detectors are given by two electromagnetic calorimeters (PHOS and EMCal). All of those detectors expect HMPID, PHOS and EMCal cover the full azimuth angle. The concrete specifications are given in Tab. 1. [17]

Detector	Acceptance (η, ϕ)	Position (m)	Dimension (m^2)	Channels
ITS layer 0	± 2.5	0.0224,0.0261	0.0421	108
ITS layer 1	± 2.3	0.0301,0.0346	0.0562	144
ITS layer 2	± 2.0	0.0378,0.0421	0.0702	180
ITS layer 3	± 1.5	0.1944,0.1977	1.0483	2688
ITS layer 4	± 1.4	0.2439,0.2470	1.3104	3360
ITS layer 5	± 1.4	0.3423,0.3454	3.2105	8232
ITS layer 6	± 1.3	0.3918,0.3949	3.6691	9408
TPC	± 0.9 at $r = 2.8m$	0.848,2.466	readout 32.5	557 568
	± 1.5 at $r = 1.4m$		Vol. 90 m^3	
TRD	± 0.84	2.90,3.68	716	1.2 M
TOF	± 0.9	3.78	141	157 248
HMPID	$\pm 0.6, 1.2° < \phi < 58.8°$	5.0	11	161 280
PHOS	$\pm 0.12, 220° < \phi < 320°$	4.6	8.6	17 920
EMCal	$\pm 0.7, 80° < \phi < 187°$	4.36	44	12 672
ACORDE	$\pm 1.3, -60° < \phi < 60°$	8.5	43	120

Table 2: Geometric specifications of the detectors of ALICE [17] with updated ITS2 [5]

2.2 Central Detectors

As already stated, the two innermost detectors of the central barrel are given by the upgraded Inner Tracking System (ITS2) and the Time Projection Chamber (TPC). Those two are of particular importance for this thesis, as the simulations and data gathering for the investigation of the particles is done solely with them.

2.2.1 ITS2

The Inner Tracking System (ITS) is the innermost part of the ALICE detector. In 2021, the ITS system was fully replaced by an updated version. The new ITS2 layout is given by seven layers, which geometric specifications are given in Tab. 2. They are separated into 2 barrels, the Inner and the Outer Barrel. The Inner Barrel consists of the three innermost layers 0–2 and the Outer Barrel therefore contains the remaining layers 3–6. The ITS layers itself are separated into azimuthal segments in units named staves. They are mechanically independent and fixed to a support structure, which are half-wheel shaped, to form the Half-Layers. All of those layers consist of Monolithic Active Pixel Sensors (MAPS) [5] The ITS is mainly responsible for reconstructing the primary vertices [17] and in the case of this thesis, will also be used to reconstruct the momentum of the primary particles [19].

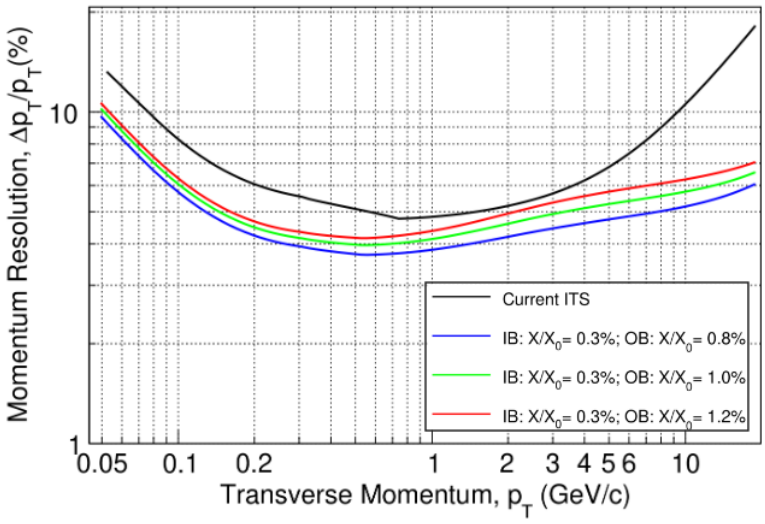

Figure 6: ITS standalone tracking transverse momentum resolution for charged pions as a function of p_T for the old ITS and different material budget options for the upgraded detector ITS at 0.5 T. For 1 GeV/c and below, the resolution is roughly 1%[5].

The new ITS2 has reduced the material budget of the first detection layer, particularly through the use of MAPS, significantly lowering the multiple scattering and energy loss effects, which should give rise to a better ITS standalone momentum reconstruction and more particles reaching the TPC, which is particularly important for the PID at low momentum.

2.2.2 TPC

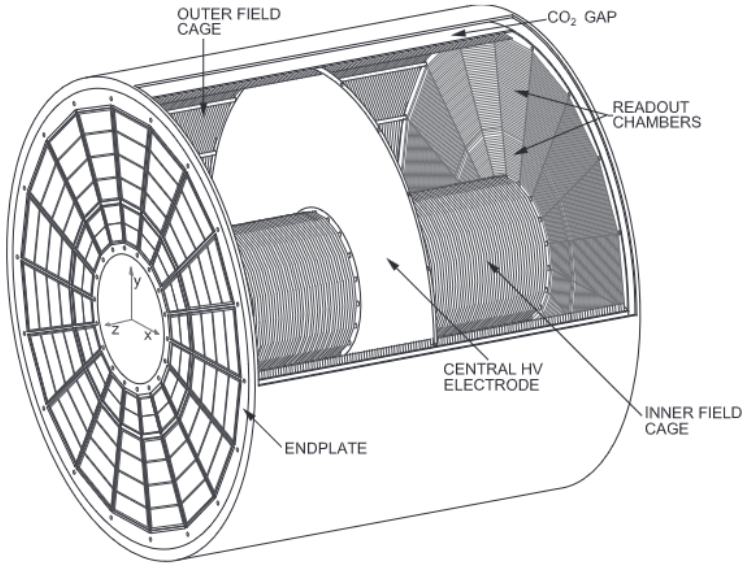

Figure 7: Schematic view of the TPC [20]

Following the ITS, the Time Projection Chamber (TPC) is the second innermost detector. It is the main tracking detector and is used for charged-particle momenta and vertex determination. Moreover, it is capable of measuring the differential energy loss dE/dx of charged traversing

particles. In principle, the TPC is a cylindrical gas chamber, with a field cage to provide a uniform electrostatic field. When charged particles traverse the gas chamber filled with 90% Ne and 10% CO_2, they will leave a track of ionized gas molecules. Those ionized electrons will drift, due to the electrostatic field, to the position and time sensitive readout pads on the end plates of the TPC cylinder, which results in the track reconstruction of the traversing particles [21].

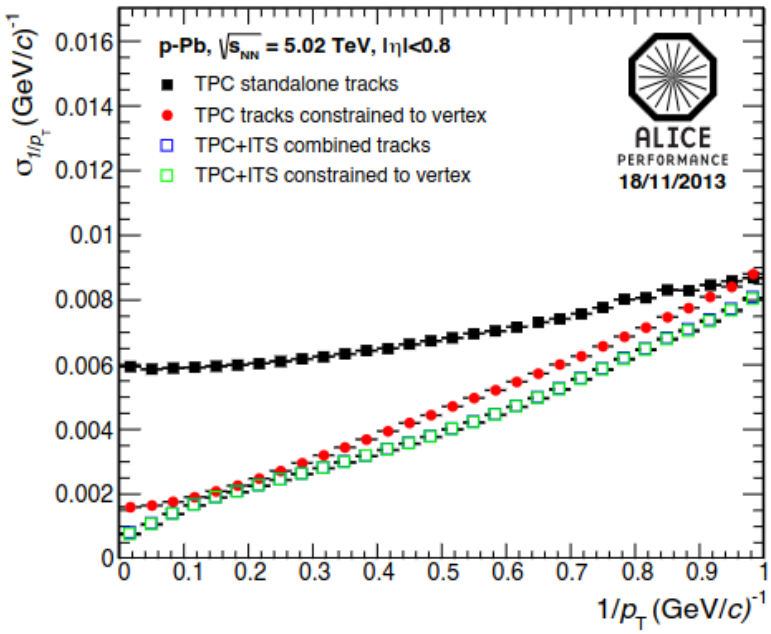

Figure 8: Resolution in $1/p_T$ as a function of $1/p_T$ for the ALICE central barrel. The plot shows the $1/p_T$ resolution for TPC standalone tracks and for global tracks combining tracking in ITS and TPC with and without vertex constraint. The data is from p–Pb collisions collected in 2013 at 0.5 T. [20].

3 Simulation

To investigate the properties of low-momentum protons, kaons, and pions within the ALICE detector, a simulation of the two innermost detectors, namely the ITS2 and TPC, was conducted. As an initial step into this unexplored momentum regime, a highly simplified setup using a standalone Geant4 simulation was employed. The decision to forego the more complex O2 framework for ALICE [22] was made to keep the study manageable within the scope of a bachelor's thesis, which is intended as an exploratory feasibility study. While this simplified approach enabled faster simulations, it also introduced significant limitations. For instance, the exact detector geometry and readout mechanisms of the ITS2 and TPC were not modelled. As a result, effects such as charge distortions within the TPC [23], overlapping events in the readout frame, and missing material like the beam pipe were not accounted for. These factors will likely lead to differences in the results when more detailed simulations are conducted. Therefore, the findings presented here should be regarded as preliminary guidance, providing insight into whether more sophisticated and comprehensive studies should follow.

3.1 Geant4

Geant4 is an open source software framework to simulate various particles and their passage through matter. It covers the physics of photons, electrons muons, hadrons and ions from meV up to several TeV. Therefore, it is used in many fields such as medical physics, high energy astrophysics and accelerator physics [24].

3.1.1 Structure of simulation

The main framework of the simulation was done with Geant4 by Andrés Bórquez. The simulation is set to inject pions, kaons and protons with their respective antiparticles into a simulation of the ITS2 and TPC of ALICE, under none or low magnetic field. Therefore, each simulated event includes 12 particles with each 2 particle-antiparticle-pairs of the pion, kaon and proton [25]. For the whole analysis 10^6 of those events were generated, resulting in $1.2 \cdot 10^7$ primary particles.

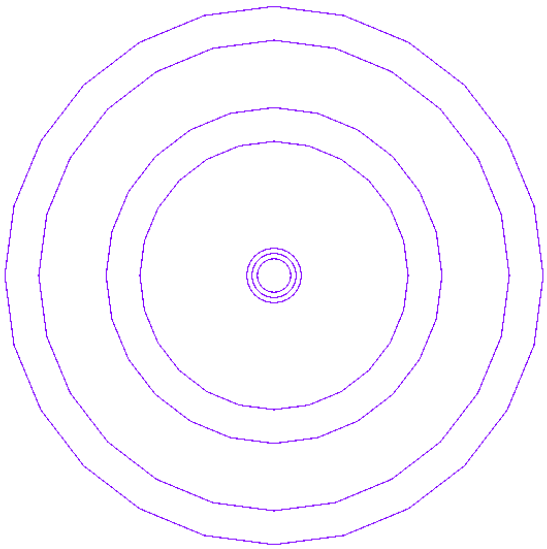

Figure 9: Visual representation of the ITS2 layers in the Geant Setup.

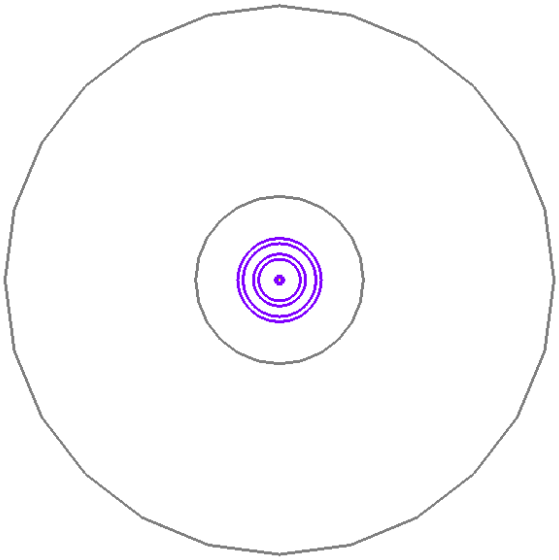

Figure 10: Visual representation of the TPC layers in the Geant Setup.

In Figs. 9 and 10, the schematics of the simulation are shown. As already hinted in the introduction of the chapter, the ITS2 and TPC simulations have many simplifications. The ITS has seven layers of silicon with the thickness and radius as given in [5], so the material budget is accurately simulated at 0.3 %. The TPC is a gas chamber filled with 90/105 parts Ne, 10/105 pars CO_2 and 5/105 parts N^2 and no readout pads. To account for this, the maximum hit distance is set to 4 mm, so that a similar amount of hits to a high momentum charged particle is obtained (Fig. 62). The empty space around the detector units is filled with air.

3.2 Simulation properties

Before starting the simulation the framework needs to be set, meaning a lower and upper limit for the momentum of the injected particles has to be chosen at which a reasonable detection and therefore classification is possible, up to the region of already reconstructed particles at ALICE and a magnetic field needs to be chosen, which ensures a balance between particles reaching the TPC and the magnitude of reconstruction error of the transverse momentum.

3.2.1 Injected particles

To be able to classify the primary particles, the momentum of the primary particle and its path have to be reconstructable, to ensure a reliable primary vertex reconstruction. For this, the charged kaons, charged pions, protons and anti-protons have to traverse the ITS2. This means that the lower momentum limit needs to be low enough so that the least energetic particles won't fulfil this condition at all (Fig. 11), to ensure the whole spectrum of possibly reconstructable low momentum particles is covered with the analysis. To determine the lower momentum limit,

preliminary simulations were done, to see at which point the fraction of particles traversing the ITS vanishes.

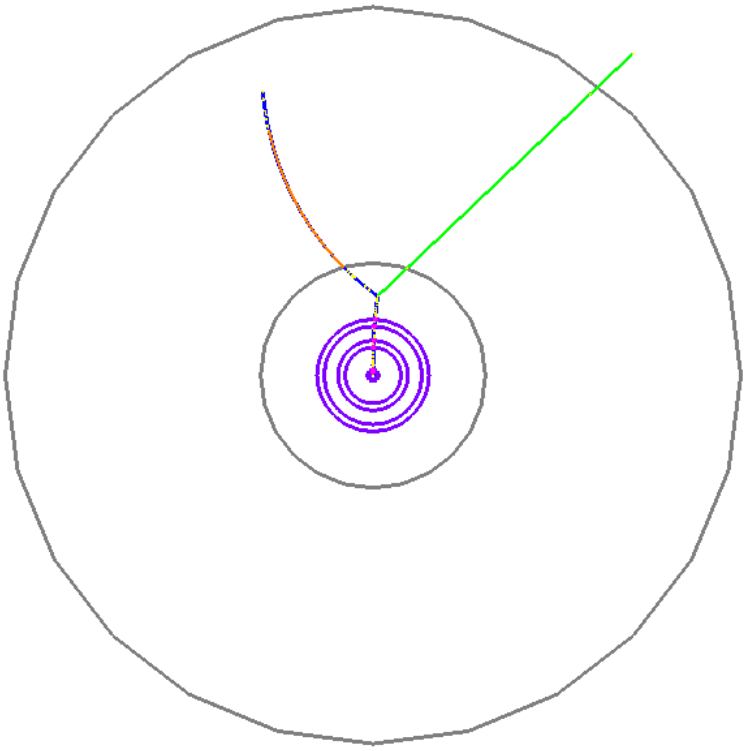

Figure 11: Example of a pion not reaching the TPC due to early decay into a muon (orange) and an anti neutrino.

Particle	Lower p_T limit [MeV/c]	Upper p_T limit [MeV/c]	Azimuthal angle [rad]	Rapidity [rad]
$\pi^{\pm}$	20	150	0–2π	-1.25–1.25
$K^{\pm}$	75	250	0–2π	-0.85–0.85
$p, \overline{p}$	125	350	0–2π	-0.7–0.7

Table 3: transverse momentum, rapidity and azimuthal limits for the injected particles

The momentum limits for the particles can be found in Tab. 3. The upper limits are set 50 MeV/c higher than the current threshold of the lowest classified particles, as everything above this momentum is not of interest for this thesis, because the methods for their PID are already existing and working.
Each of the injected particle has a transverse momentum p_T drawn from a uniform distribution over the region from Tab. 3 and a rapidity η and azimuthal angle ϕ uniformly drawn from Tab. 3. Those values then yield the momentum of the particle:

$$\vec{p} = (p_T \cos(\phi), p_T \sin(\phi), m_T \sinh(\eta)) \tag{8}$$

with the transverse mass m_T

$$m_T = \sqrt{m^2 + p_T^2} \tag{9}$$

with the particle's mass m.

3.2.2 Selection of the magnetic field strength

In order to find a suitable magnetic field strength, the limitations must first be identified so that an optimum magnetic field can be determined using these limitations. On one hand, the magnetic field needs to be low enough for the charged particles to actually reach the TPC, as one can see in Fig. 12.

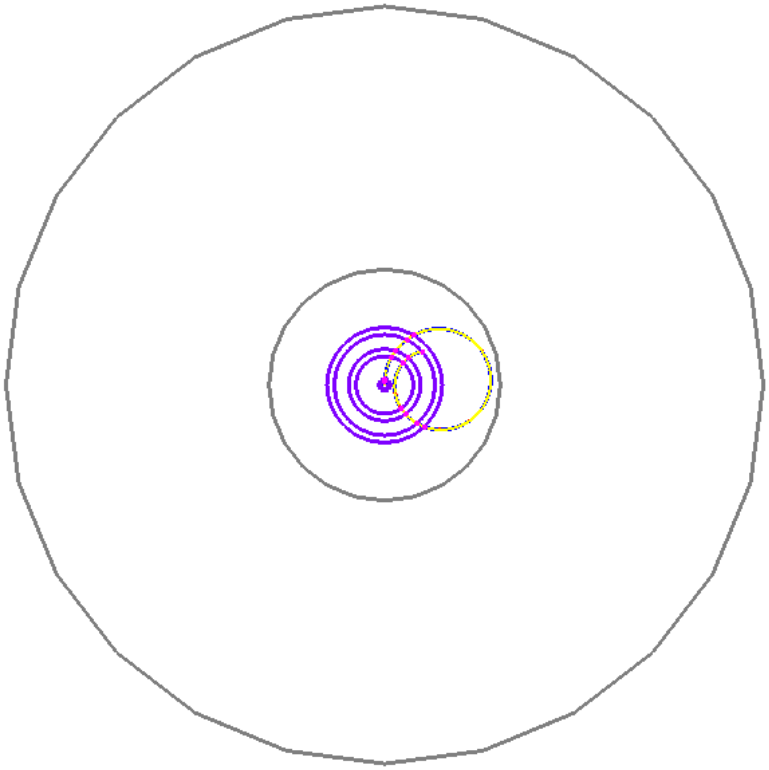

Figure 12: Example of a charged particle not reaching the TPC due to too much curvature induced by the magnetic field

On the other hand, the magnetic field is used as later explained for the reconstruction of the transverse momentum. This means the chosen magnetic field strength for the simulation should lead to the lowest possible reconstruction error in the transverse momentum, defined as

$$\sigma_{rec} = \frac{|x_{true} - x_{rec}|}{x_{true}}, \tag{10}$$

with the true value x_{true} and the reconstructed value x_{rec}, while still respecting the first restriction. Two factors primarily influence the reconstruction error. First, multiple scattering, which scales inversely with the magnetic field strength ($\propto B^{-1}$), becomes more significant at lower magnetic fields. Second, a higher magnetic field increases the curvature of the particle's

trajectory, leading to greater energy loss, which however could be accounted for by energy loss corrections.
Therefore, preliminary simulations with magnetic fields between 0 and 0.4 T were done and both the fraction of particles reaching the TPC (1st restriction) and the reconstruction error of the transverse momentum (2nd restriction) in the TPC and the ITS have been evaluated and plotted against the magnetic field strength in Fig. 13, 14.

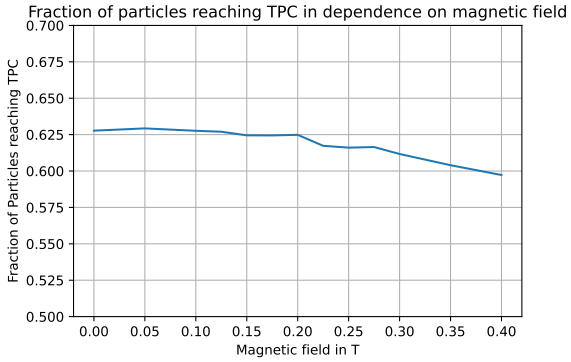

Figure 13: Fraction of particles reaching the TPC

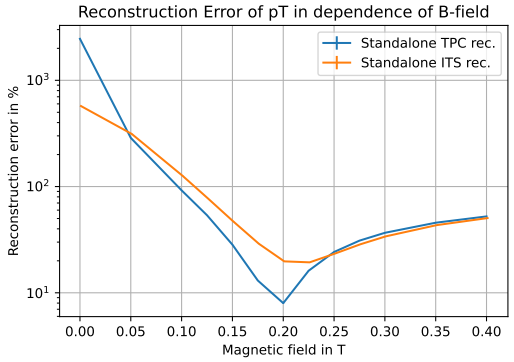

Figure 14: Reconstruction error of standalone ITS and TPC tracks

As one can see in Fig. 13, the magnetic field has in boundaries between 0 and 0.4 Tesla no big effect on the particles actually reaching the TPC, which means, that the particles, thats momentum is low enough to be affected enough by the curvature, wouldn't reach the TPC due to energy loss or decay anyway. On the other hand, the reconstruction error shown in Fig. 14 shows a strong dependence on the magnetic field, with a clear minimum around 0.2 Tesla. This finding is consistent with the fact that other low momentum analyses have already been carried out at 0.2 Tesla [26], showing that the simulation setup, although simplified, is capable of producing results close to the real properties. Therefore, for all following simulations and analysis, a magnetic field strength of 0.2 Tesla was chosen.

3.3 Readout of simulation

This simulation is not done by the generation of the whole particle collision process, but only by injecting pions, kaons and protons with a fixed initial momentum. This is then used, with the set magnetic field, to process the trajectories. In total, there are 3 different data files saved from the simulation, with the information shown in Tab. 4, 5 and 6.

Feature	Unit
trackID	-
layer number	-
x-position	cm
y-position	cm
z-position	cm

Table 4: ITS Data

Feature	Unit
trackID	-
x-position	cm
y-position	cm
z-position	cm
deposited energy	MeV

Table 5: TPC Data

Feature	Unit
trackID	-
PDG code	-
Parent ID	-
charge	-
initial P_x	MeV/c
initial P_y	MeV/c
initial P_z	MeV/c
deposited energy	MeV

Table 6: True Data

4 Machine Learning Introduction

4.1 Introduction

A computer program classified as Machine Learning (ML) learns from experience E with respect to some class of task T and performance measure P, if its performance at tasks in T, as measured by P, improves with experience E [27]. This principle can be and is used in modern particle physics in addition to conventional methods to classify particles from the detector data and maybe even improve its efficiency and accuracy. To investigate the potential benefits in fields of low momentum classification at ALICE, firstly the used software and algorithm have to be introduced.

4.2 XGBoost

XGBoost ("Extreme Gradient Boosting") is a software library designed to implement machine learning algorithms under the gradient boosting framework, where gradient boosting is a type of boosted trees [28].

4.3 Decision Tree

A decision tree is a model, which gives a prediction $\hat{y}$ outgoing from n examples with m features, which are all classified by a target y. The prediction therefore tries to use the features of the training examples, to find a pattern to predict the target of those training examples with the highest possible accuracy.
To measure the performance of the classifier, one has to construct an objective function. This usually consists of the training loss $L(\theta)$ function, which measures, how predictive the model is in respect to the training data and a regularization term $\Omega(\theta)$, which is used to prevent overfitting, which in case of a decision tree would mean, that it prevents the tree from being too complex.

$$\text{obj}(\theta) = L(\theta) + \Omega(\theta) \tag{11}$$

A normal choice for the loss function would be for example

$$L(\theta) = \sum_i (y_i - \hat{y}_i)^2 \tag{12}$$

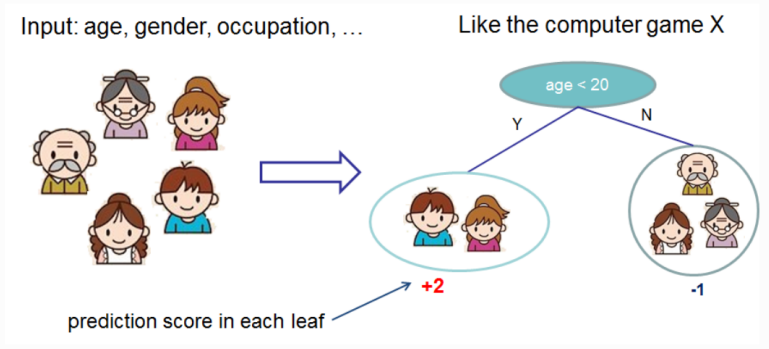

Figure 15: Visual representation of a Tree [28]

4.4 Tree Ensembles

XGBoost uses a decision tree ensemble as the classification model. It consists of a set of Classification and Regression Trees (CART). Therefore, the predictions scores of each individual tree are summed up, and the average is taken for the final prediction.

$$\hat{y} = \sum_{k=1}^{K} f_k(x_i), f_k \in F, \tag{13}$$

where K is the number of trees and f_k is a function from the set of all CARTs. This leads to the objective function

$$\text{obj}(\theta) = \sum_{i}^{n} l(y_i, \hat{y}_i) + \sum_{k=1}^{K} \omega(f_k), \tag{14}$$

where $l(y_i, \hat{y}_i)$ is the loss function of the prediction and $\omega(f_k)$ is the regularization for each tree, to prevent overfitting.

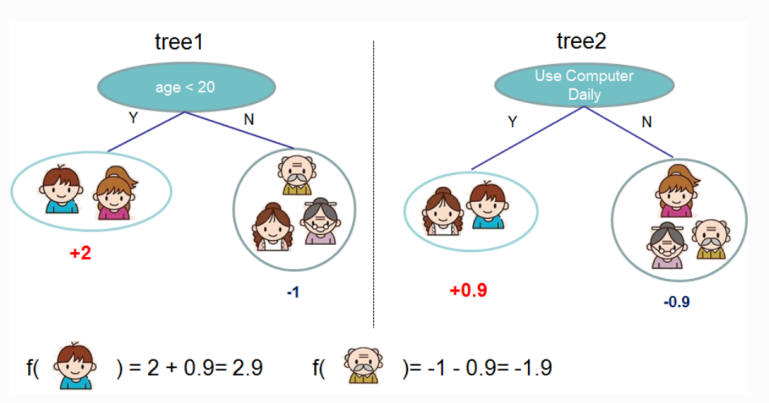

Figure 16: Visual representation of a Tree Ensemble [28]

4.5 Tree Boosting

Lastly, the introduced model and therefore the objective function has to be optimized.

$$\text{obj}(\theta) = \sum_{i}^{n} l(y_i, \hat{y}_i^{(t)}) + \sum_{k=1}^{K} \omega(f_k), \tag{15}$$

where $\hat{y}_i^{(t)}$ is the prediction of tree i in the optimization step t

$$\begin{aligned} \hat{y}_i^{(0)} &= 0 \\ \hat{y}_i^{(1)} &= \hat{y}_i^{(0)} + f_1(x_i) \\ \hat{y}_i^{(2)} &= f_1(x_i) + f_2(x_i) = \hat{y}_i^{(1)} + f_2(x_i) \\ &... \\ \hat{y}_i^{(t)} &= \sum_{k=1}^{t} f_k(x_i) = \hat{y}_i^{(t-1)} + f_t(x_i) \end{aligned} \tag{16}$$

This leads to the objective function in the t-th step of the trees

$$\begin{aligned} \text{obj}^{(t)} &= \sum_{i}^{n} l(y_i, \hat{y}_i^{(t)}) + \sum_{i=1}^{t} \omega(f_i) \\ &\sum_{i}^{n} l(y_i, \hat{y}_i^{(t-1)} + f_t(x_i)) + \omega(f_t) + \text{const.} \end{aligned} \tag{17}$$

Now the second order Taylor expansion is taken for the loss function:

$$\text{obj}^{(t)} = \sum_{i}^{n} [l(y_i, \hat{y}_i^{(t-1)}) + g_i f_t(x_i) + \frac{1}{2} h_i f_t^2(x_i)] + w(f_t) + \text{const}, \tag{18}$$

where

$$\begin{aligned} g_i &= \partial_{\hat{y}_i} l(y_i, \hat{y}_i^{(t-1)}) \\ h_i &= \partial_{\hat{y}_i}^2 l(y_i, \hat{y}_i^{(t-1)}) \end{aligned} \tag{19}$$

By removing all constants, this leads to the specific objective function at step t:

$$\text{obj}^{(t)} = \sum_{i}^{n} [g_i f_t(x_i) + \frac{1}{2} h_i f_t^2(x_i)] + w(f_t) \tag{20}$$

Ultimately, we have to define the complexity of the trees, to get the regularization term with:

$$\omega(f) = \gamma T + \frac{1}{2} \lambda ||\omega||^2. \tag{21}$$

Where T is the number of leaves and ω is the vector of scores on the leaves. With that in mind and $f_t(x) = \omega_{q(cx)}$ where $q(x)$ is a function that assigns the data points to the correct leaves, we get

$$\begin{aligned} \text{obj}^{(t)} &\approx \sum_{(i=1)}^{n} [g_i \omega_{q(x_i)} + \frac{1}{2} h_i \omega^2_{q(x_i)}] + \gamma T + \frac{1}{2}\lambda \sum_{(j=1)}^{T} w_j^2 \\ &= \sum_{j=1}^{T} [(\sum_{i \in I_j} g_i)\omega_j + \frac{1}{2}(\sum_{(i \in I_j)} h_i + \lambda)\omega_j^2] + \gamma T, \end{aligned} \tag{22}$$

where $I_j = i|q(x_i) = j$ is the set of indices of the data points at leave j. With $G_j = \sum_{i \in I_j} g_i$ and $H_j = \sum_{i \in I_j} h_i$, this simplifies to

$$\text{obj}^{(t)} = \sum_{j=1}^{T} [G_i \omega_j + \frac{1}{2}(H_i + \lambda)\omega_j^2] + \gamma T \tag{23}$$

As each w_j is independent, we have a quadratic function, which has its optimum at

$$\begin{aligned} \omega_j^* &= -\frac{G_j}{H_j + \gamma} \\ \text{obj}^* &= -\frac{1}{2} \sum_{j=1}^{T} \frac{G_j^2}{H_j + \lambda} + \gamma T \end{aligned} \tag{24}$$

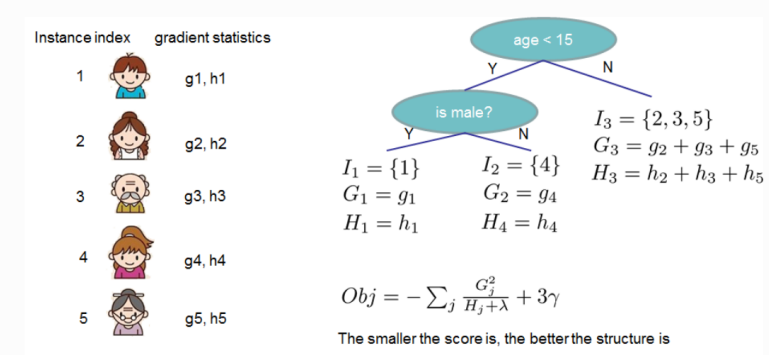

Figure 17: Scoring system of a Tree up to second order Taylor [28]

With obj* we know have a function to measure how good the optimal tree at a certain complexity is. We can measure, if it is reasonable to split a certain leaf of a certain tree by subtracting both objective functions from each other. We get:

$$\text{Gain} = \text{obj}^*_{unsplit} - \text{obj}^*_{split} = \frac{1}{2}\left[\frac{G_L^2}{H_L + \lambda} + \frac{G_R^2}{H_R + \lambda} - \frac{(G_L + G_R)^2}{H_l + H_R + \lambda}\right] - \gamma, \tag{25}$$

As we can see, if the score is smaller than γ, we should not split the tree at this certain leave.

This will be iterated over all leaves from all trees, until the gain of every split is smaller than γ. [28]

5 Data Reconstruction

For the PID, we will need a variety of properties from the particles. Those properties can be reconstructed with the information we get from the TPC and the ITS2. The following chapter focusses on the methodology of the different reconstructions, of which an overview is given in Tab. 7.

Quantity	Unit	Reconstruction
Transverse momentum p_T	MeV/c	Circle fit
z-momentum p_z	MeV/c	Helix fit
Total momentum p	MeV/c	Comb. of p_T and p_z
Differential Energy loss dE/dx	MeV/cm	Energy deposition and hit position
charge Q	-1,1	Helix orientation
Primary	boolean	DCA

Table 7: Overview of reconstructed properties and their methods

5.1 Momentum Reconstruction of Charged Particles

The momentum p of a particle in the presence of a magnetic field can be systematically reconstructed by considering its transverse and longitudinal components.

$$\vec{p} = \vec{p_T} + \vec{p_z} = (p_x, p_y, 0) + (0, 0, p_z) = (p_x, p_y, p_z) \tag{26}$$

Given a magnetic field oriented along the z-axis, the transverse momentum p_T lies in the xy-plane and is responsible for the helical motion of the particle, while the longitudinal momentum p_z is parallel to the field and determines the pitch of the helix.

5.2 Transverse Momentum Reconstruction

Therefore, we firstly need to reconstruct the transversal momentum, that is perpendicular to the B-field, that is applied. This is done by determining the radius of the charged particles in the B-field, which can be directly used to determine the momentum with

$$p_T = 0.3BR \tag{27}$$

where p_T is the transverse momentum in GeV/c that results from the magnetic field B in T and radius r in m. The reconstruction of the radius was done with the help of Ref. [29].

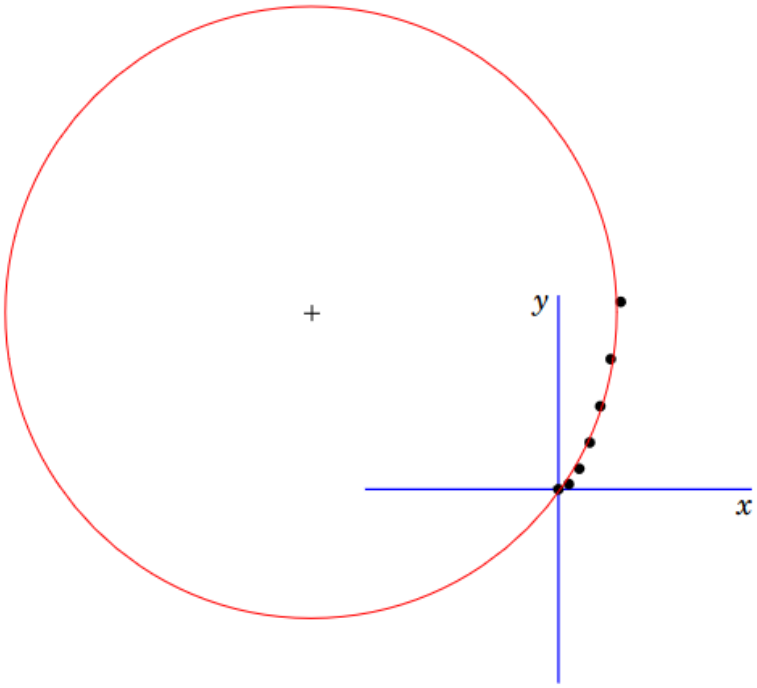

Figure 18: Schematics of the circle fit [29]

5.3 Reconstruction of the z-momentum

Next up, the total momentum of the particles needs to be reconstructed. For this, we can use the already reconstructed radius and circle center from the previous step and fit a helix function to the TPC hits

$$f(z) = (x_c + r\cos(\omega z + \varphi), y_c + r\sin(\omega z + \varphi), z) \tag{28}$$

with the free parameters ω and φ. The estimator ω leads with the equation

$$\phi = \arctan\left(\frac{1}{\omega r}\right) \tag{29}$$

to the angle between the transverse momentum p_T and the total momentum p. The whole momentum p then results from

$$p = \sqrt{p_T^2 + p_z^2} \tag{30}$$

with

$$p_z = p_T \tan(\Phi) = \frac{p_T}{\omega r} \tag{31}$$

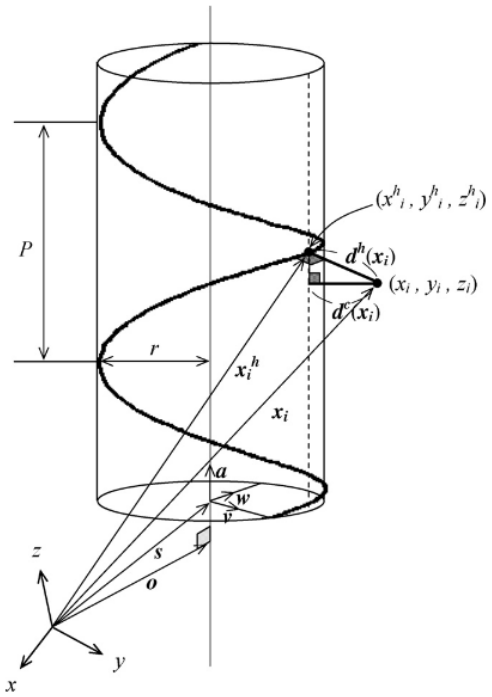

Figure 19: Schematics of the helix fit [30]

5.4 Charge Reconstruction

To obtain the charge of a particle, one has to look at the helix fit reconstruction. Depending on the sign of the charge, the magnetic field will lead to different orientations of the circular motion, meaning the particle will either rotate in a positive or negative handed manner, as the force

$$F = q(\vec{v} \times \vec{B}) \tag{32}$$

with the charge q, the particle's velocity v and the magnetic field B, changes signs according to the charge, which will lead to a different sign in the cyclotron frequency ω_c

$$\omega_c = \frac{qB}{m} \tag{33}$$

with the charge of the particle q, the magnetic field B and the mass of the particle m. As we only know the chronological order of our hits and do not have a direct time resolution, we do not directly fit w_c dependent on the time, but w_{fit} dependent on the z position of the hits, as seen in Eq. (28). But as they are chronological ordered, it will lead to the same orientation, when multiplied by the sign of the z momentum:

$$\text{sign}(\omega_c) = \text{sign}(\omega_{fit}) \cdot \text{sign}(p_z) \tag{34}$$

As a negative charge will lead to a counterclockwise rotation in the xy-plane, which is the mathematically positive direction, the sign of the charge is reconstructed by:

$$\text{sign}(Q) = -\text{sign}(\omega_{fit})\text{sign}(p_z) \tag{35}$$

5.5 Primary Vertex Reconstruction

To decide, whether a particle is a primary particle (emerges directly from the collision) or is a secondary particle (e.g. the decay of a primary particle) one needs to calculate the Distance of Closest Approach (DCA) to the collision point, or in our case, as the particles are injected, to the origin of injection $\vec{x}_{\text{origin}} = (0, 0, 0)^T$.
As the helix motion of the particles is already reconstructed, we are able to extrapolate the helix function f(z) of the particles, to see, how close it gets to the origin, by minimizing:

$$\text{dist}(f(z), \vec{x}_{\text{origin}}) = \sqrt{(r\cos(\omega z + \varphi) - x_c)^2 + (r\sin(\omega z + \varphi) - y_c)^2 + z^2} \tag{36}$$

with x_c and y_c being the center points of the rotation in the xy-plane. When the particle's Point of Closest Approach (PCA) to the origin is small enough, it will be flagged as a primary particle.

5.6 Differential Energy Loss

Now that we have the reconstructed momentum of the particles, we only need the differential energy loss dE/dx to determine the particle ID via a Bethe-Bloch fit. The differential energy loss is determined by using the data of the deposited energy and the distance to the prior hit and averaging over the hits of a particle.

$$\left[\frac{dE}{dx}\right] = \frac{1}{n_{\text{hits}}} \sum_{i}^{n_{\text{hits}}} \frac{(\text{energy deposition})_i}{(\text{distance to prior hit})_i} \tag{37}$$

The calculated differential energy losses will follow a Landau distribution, which does not have a finite first or second order moment, what makes it really unreliable to calculate an average due to large fluctuations. A widely used solution is the truncation of the highest values before taking the mean, by only using the α lowest values. This method is called a truncated mean estimator and was empirically proven to yield good results.

$$\left[\frac{dE}{dx}\right]_{\text{trunc}} = \frac{1}{\alpha n_{\text{hits}}} \sum_{i}^{\alpha n_{\text{hits}}} \frac{(\text{energy deposition})_i}{(\text{distance to prior hit})_i} \tag{38}$$

The truncated mean results follow approximately a Gaussian distribution with a well-defined first and second order moment. Typical values for α range from 0.5 to 0.7 [31].

6 Reconstruction Results

6.1 ITS Reconstructions

The ITS2, being the innermost detector unit of ALICE is especially important for the very low momentum particles, as they suffer from significant energy loss and particles that decay before the TPC might still be investigated by their decay products, if the ITS provides good enough momentum and track reconstruction. Therefore, the momentum reconstruction was analysed in the following part. Before the analysis, some particles were cut by only allowing reconstruction, that have a $\chi^2_{red} < 5$ and have at least 5 ITS hits.

6.1.1 Transverse Momentum

As mentioned in Section 5.2, a simple circle fit was used to determine the transverse momentum via its radius in the magnetic field. For the ITS2, at least 5 hits were used for the reconstruction. The results of the reconstruction can be seen in Figs. 20, 21, 22.

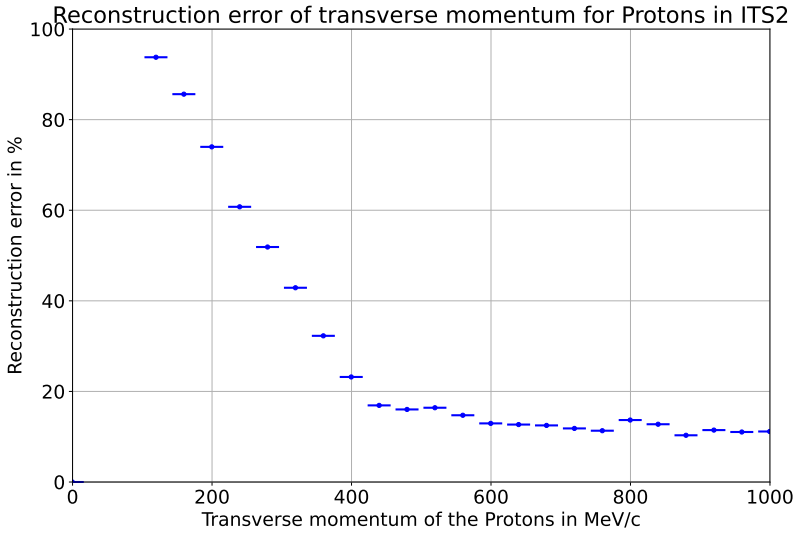

Figure 20: Reconstruction error of the transverse momentum of standalone ITS2 reconstruction of protons.

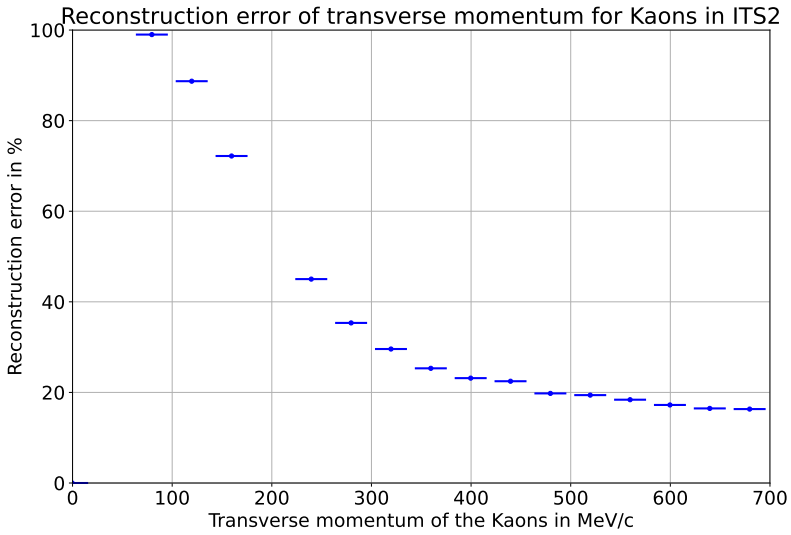

Figure 21: Reconstruction error of the transverse momentum of standalone ITS2 reconstruction of kaons.

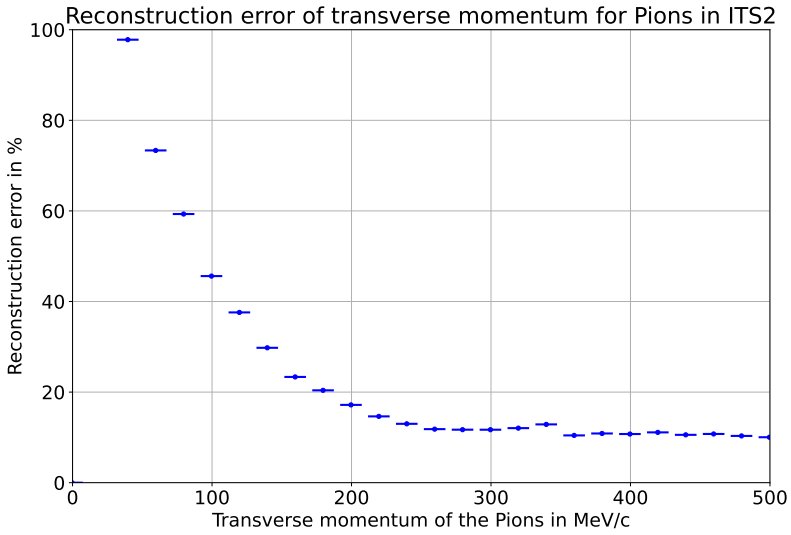

Figure 22: Reconstruction error of the transverse momentum of standalone ITS2 reconstruction of pions.

As one can see for all three particle species, the ITS2 standalone p_T reconstruction does not work very well in the lowest momentum regime, but stabilizes for protons at around 400 MeV/c, for pions at around 200 MeV/c with a reconstruction error of about 8 % and for kaons at around 300 MeV/c with about 18 %. The momentum resolution for pions is consistent with the expected one from Fig. 6, where the resolution is about 4 %. The two times higher resolution in the simulated ITS2 can be explained by higher multiple scattering effects due to the lower magnetic field $\propto \beta^{-2}$. However, below 200 MeV/c, the simulation yields significantly higher

reconstruction errors. This discrepancy indicates, that either the reconstruction methods or the simulation is faulty. As in Fig. 6 a Kalman filter tracking technique was used, it is likely, that the simplified p_T reconstruction with a circle fit begins to fail at those low momenta due to significant multiple scattering. Therefore, with a more sophisticated reconstruction, it can be expected, that also the low momentum region should be consistent with the findings of the technical design report of the ITS2 [5].

As we get stable results after a certain momentum threshold, this indicates, that the reconstruction with a simple circle fit works for higher momentum particles just fine, but at low momentum there is some kind of disturbance, which leads to a larger reconstruction error. The growing reconstruction error is attributable to multiple scattering with the air in the detector, but especially within the silicon layers of the ITS, which starts to alter the path of the particles more severely, as they get less energetic, which also explains the constant rise as we get into lower momenta of the particles.

This can be seen in a scatter plot between the true transverse momentum and the ITS reconstructed transverse momentum of protons in Fig. 23, as the mean reconstruction lies pretty much on the true value with a shift to an underestimation of the momentum at low momenta due to energy loss.

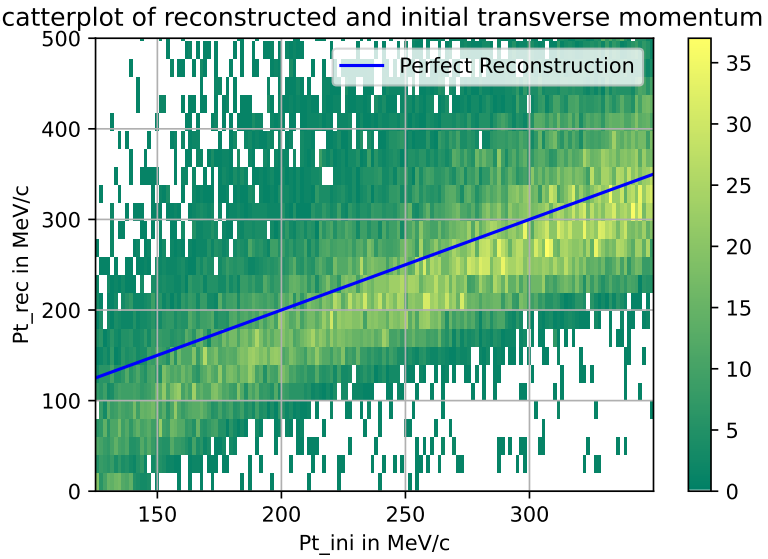

Figure 23: Scatter plot between the reconstructed and true transverse momentum for protons.

6.2 TPC Reconstructions

The TPC, positioned as the second innermost detector at ALICE, is the first detector capable of measuring energy deposition, which is crucial for PID. Like for the ITS2, the momentum resolution is investigated, but furthermore other key properties are reconstructed and checked, as the ITS2 momentum resolution showed to be inadequate at this point, leaving the charge

and primary vertex to a standalone TPC reconstruction.
Before the analysis, as for the ITS, some cuts in the investigated data were made. Like for the ITS reconstructions, $\chi^2_{red} < 5$ and at least 5 TPC hits were required. Additionally, for the charge and momentum reconstruction, the DCA primary cut was used, as only the primary protons, kaons and pions and secondary muons are of interest.

6.2.1 Efficiency

Since low-momentum particles encounter several challenges before reaching the TPC, it is important to investigate how many particles actually reach the TPC and have a high quality reconstruction. To do this, the fraction of particles that survive the initial cuts, as outlined at the beginning of the chapter, is plotted against the transverse momentum in Figs. 24–26.

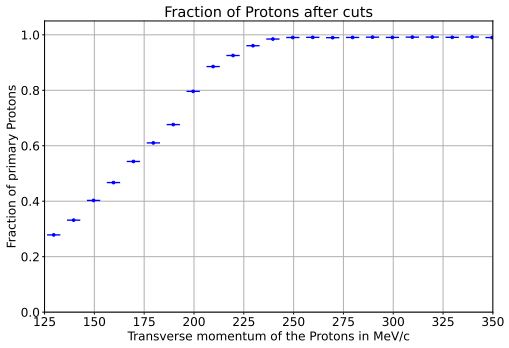

Figure 24: Fraction of protons after the cuts

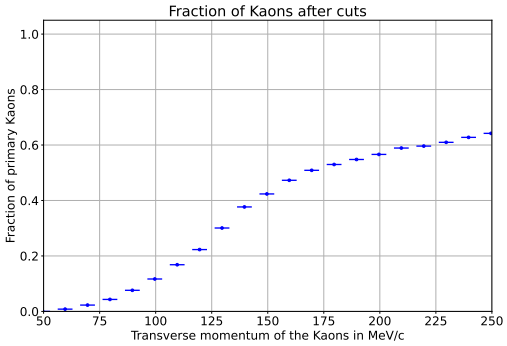

Figure 25: Fraction of kaons after the cuts

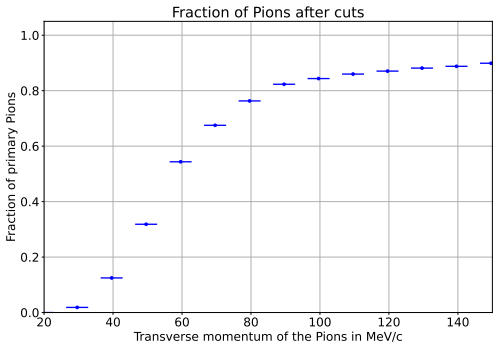

Figure 26: Fractions of pions after the cuts

As shown in Fig. 24, the fraction of protons with sufficient TPC reconstruction remains stable down to around 230 MeV/c. Below this momentum, the energy loss for protons becomes significant, preventing many from reaching the TPC, with only 25% surviving at 125 MeV/c. Since protons are the heaviest particles under investigation, they experience the greatest energy loss, especially at low momentum, where the energy loss scales as $\propto \beta^{-2}$.

The fraction of kaons follows a similar trend to that of protons, but is overall less steep. kaons not only suffer from energy loss due to their relatively high mass but also from their unstable nature, with a decay length that depends on their momentum. The combination of these two factors results in a sharp decline in efficiency around 150 MeV/c, giving kaons the lowest overall efficiency and the slowest rise in efficiency.
Pions, being the lightest primary particles in this study, experience minimal energy loss except at very low momenta. Consequently, their efficiency remains stable for a longer range, but it eventually decreases due to both energy loss and their instability. By around 30 MeV/c, almost no pions reach the TPC.
Overall, the efficiencies demonstrate that the TPC standalone reconstructions remain stable well below the momentum limits set for Run 2, as shown in Tab. 3. This suggests that Bethe-Bloch PID is likely suitable for use in this low momentum regime for protons, kaons, and pions, a conclusion that will also be supported in the upcoming PID performance comparison.

6.2.2 Transverse Momentum

As for the ITS2 momentum reconstruction, a circle fit was used for the transverse momentum, but with the restriction, that only 70 of the TPC hits were used, if they exceeded 100 TPC hits to account for the energy loss of particles, that start circling within the TPC.

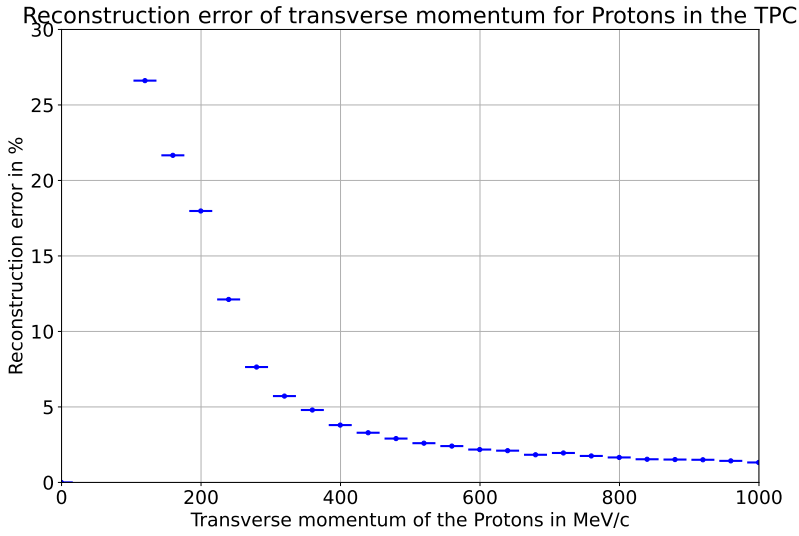

Figure 27: Reconstruction error of the transverse momentum of standalone TPC reconstruction of protons.

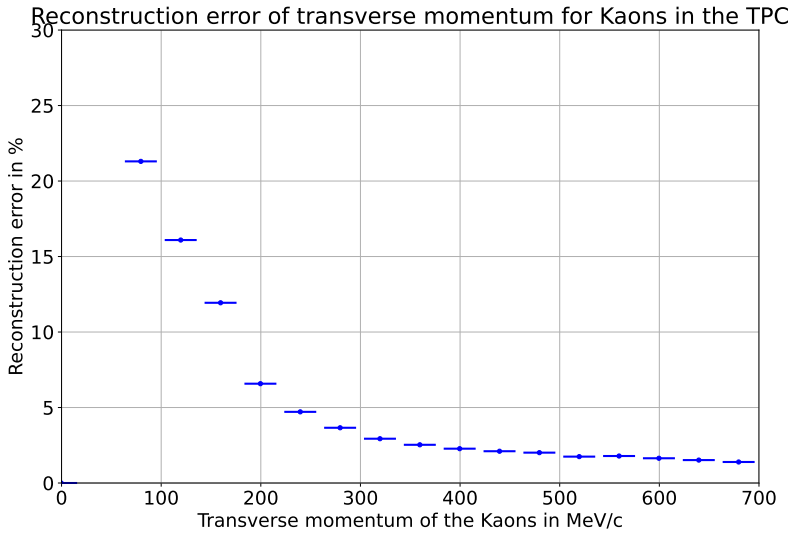

Figure 28: Reconstruction error of the transverse momentum of standalone TPC reconstruction of kaons.

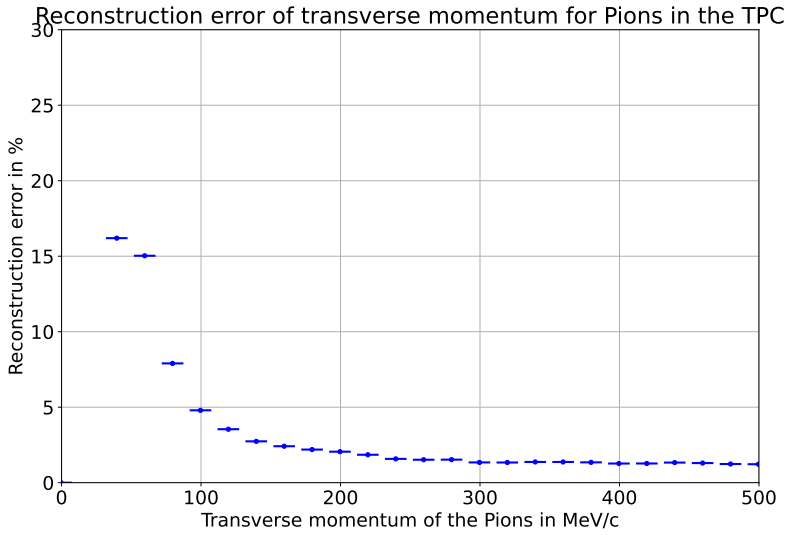

Figure 29: Reconstruction error of the transverse momentum of standalone TPC reconstruction of pions.

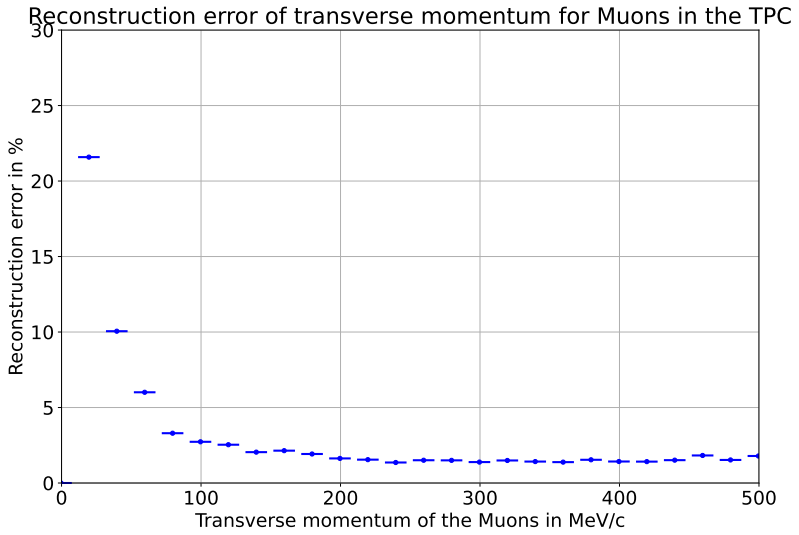

Figure 30: Reconstruction error of the transverse momentum of standalone TPC reconstruction of muons.

As one can see, the results look similar to the ITS2 reconstructions, but the overall errors are lower and the stable region with a reconstruction error is bigger, as for protons, the reconstruction error stays below 10% down to around 200 MeV/c, for kaons to 150 MeV/c and for pions down to 50 MeV/c. Moreover, the results of the higher momentum reconstruction (>400 MeV/c) show to be consistent with the performance in Fig. 8. With a resolution of around 2 % it is roughly 2 times as high, but as the multiple scattering effects should be roughly 2.5 more significant at low B-field due to the inverse scaling with the B-field ($\sigma_{MS} \propto B^{-1}$) this is expected. This shows, that the TPC simulation setup gives reasonable accurate results in terms of momentum resolution, making the study's analysis results more reliable.
Other than for the ITS2 simulation, the TPC has only a low density gas chamber without solid matter in it, which makes the scattering effects, that disturbed the ITS reconstruction, way less significant. Still, we see a significant rise in the error at low p_T. This can be explained by the fact, that we only look at primary particles for protons, kaons and pions, which have to make their way from the collision point all the way to the TPC, a way of roughly 80 cm (Tab. 2), before the first hits in the TPC are registered. This means low momentum particles, as can be seen in Fig. 42, suffer from substantial energy loss before reaching the TPC, resulting in a systematically lower reconstructed momentum, which can be seen especially well for the high mass protons.
As already stated, the scattering effects are way smaller in the TPC than in the ITS2, as the particles are traversing gas and no solid matter. Moreover, the number of TPC hits to work with is notably higher with less distance between them. This can be seen in Fig. 31, the scatter plot of the reconstructed transverse momentum from the TPC against the true transverse momentum. There is still a distribution around the true value, but way smaller than for the

ITS2.

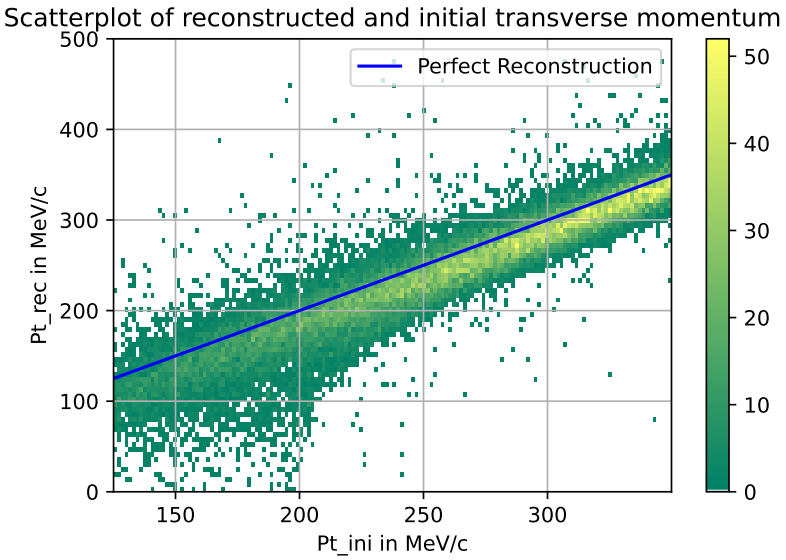

Figure 31: Scatter plot of the reconstructed and true transverse momentum for protons. As one can see, the spread of the reconstructed p_T gets higher for lower momentum protons, indicating more multiple scattering and the overall reconstruction shifts downwards below the true value, indicating significant energy loss.

6.2.3 Primary Vertex

The DCA reconstruction can now be used to determine, which particles are primaries.

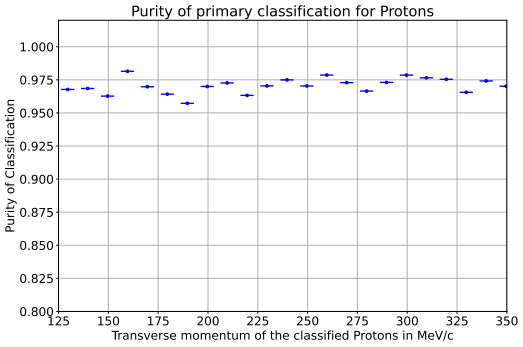

Figure 32: Purity of primary classification via DCA on protons.

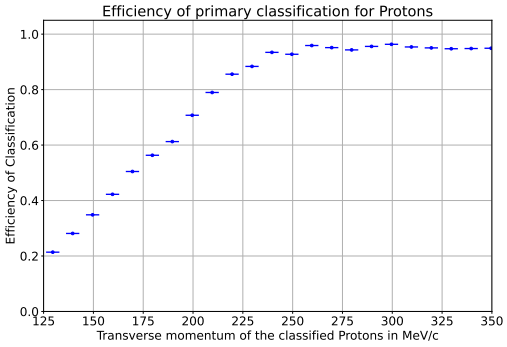

Figure 33: Efficiency of primary classification via DCA on protons.

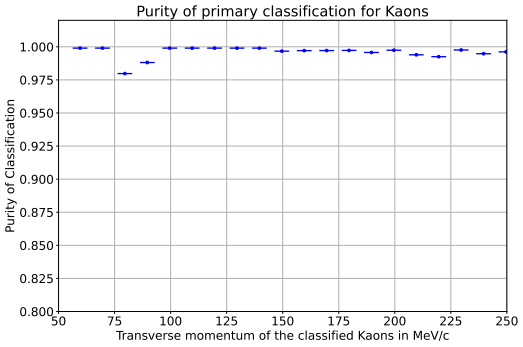

Figure 34: Purity of primary classification via DCA on kaons.

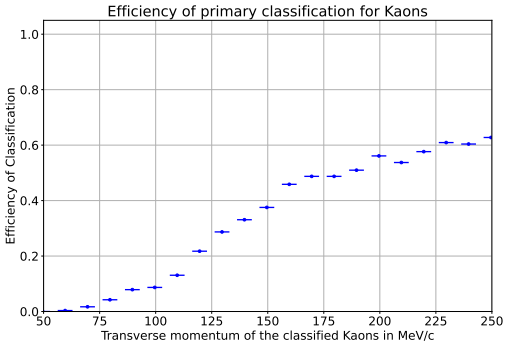

Figure 35: Efficiency of primary classification via DCA on kaons.

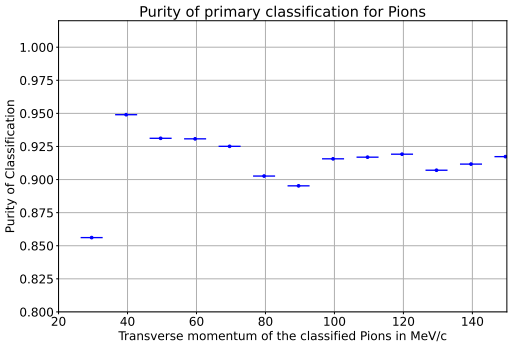

Figure 36: Purity of primary classification via DCA on pions.

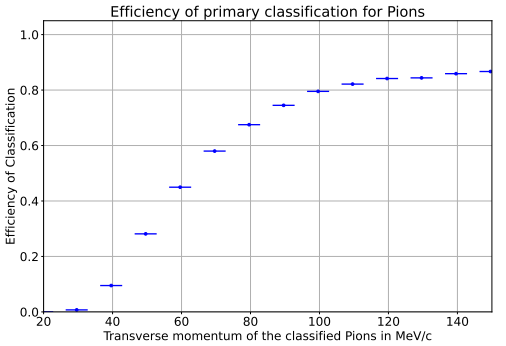

Figure 37: Efficiency of primary classification via DCA on pions.

With no significant background, the primary reconstruction shown in Figs. 32–37 encounters few issues. However, the purity of primary proton classification is slightly affected by protons knocked out from the detector material in the inner layers of the ITS2, which are mistakenly identified as primaries. The purity of pions is somewhat lower due to antiproton and proton annihilations, as well as kaon decays into charged pions near the collision point, leading to their incorrect classification as primaries. The efficiency is limited by the TPC cuts, as seen in Figs. 24–26, since the DCA was calculated using the standalone TPC helix fit.

6.2.4 Charge

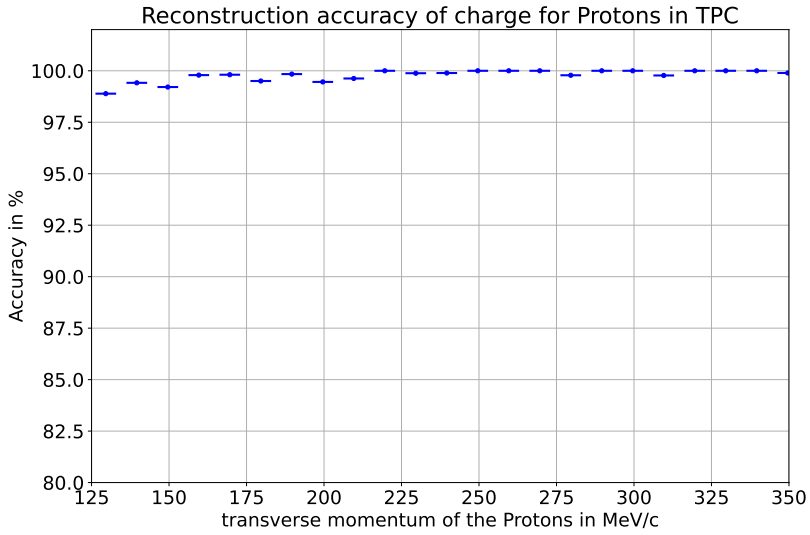

Figure 38: Reconstruction accuracy of the charge of TPC reconstruction of protons.

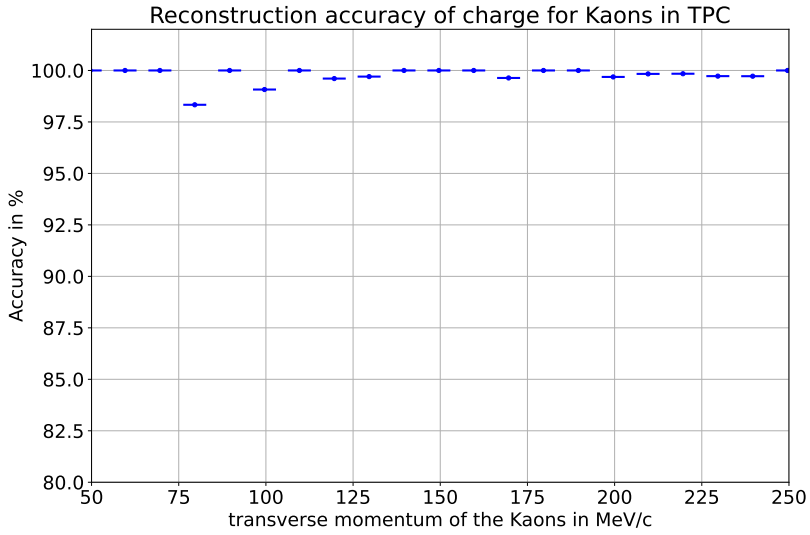

Figure 39: Reconstruction accuracy of the charge of TPC reconstruction of kaons.

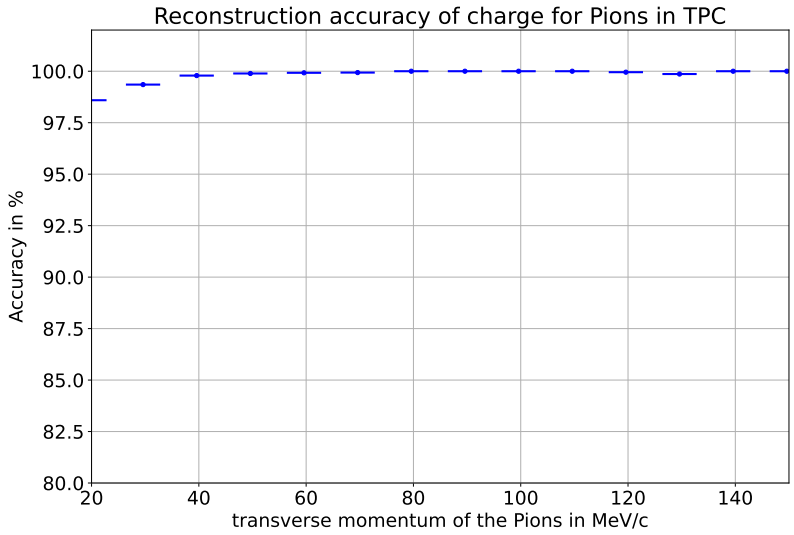

Figure 40: Reconstruction accuracy of the charge of TPC reconstruction of pions.

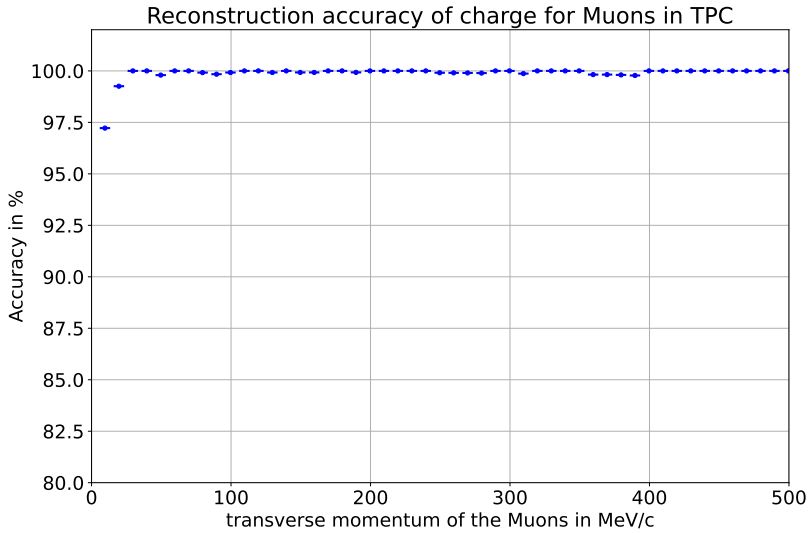

Figure 41: Reconstruction accuracy of the charge of TPC reconstruction of muons

As the charge is determined by the orientation of the helix rotation, it is very stable to the resulting error from multiple scattering and energy loss, as they do not change the orientation of the rotation. This can be seen in Figs. 38–41, as all species have a nearly perfect accuracy over the total momentum region.

6.2.5 Differential energy loss dE/dx

The differential energy loss dE/dx calculated with the truncated mean, as depicted in 5.6 cannot be subjected to an error analysis like the other quantities, as there is no true value of the differential energy loss. Still, an implicit analysis can be made by looking at the Bethe-Bloch curves of the particles, as they should be distinguishable in the low momentum region, whereby in addition the thickness of the curves gives a second measure for the accuracy of the calculation of the differential energy loss. Those curves are plotted with their respective ALEPH fits, later explained in Section 7.1, in Fig. 42. As one can see, the width of the different bands of the particles is reasonable (minimal overlap in the low momentum regime) and the ALEPH parametrizations fit well, which indicates a successful reconstruction of the differential energy loss.

7 PID methods

7.1 PID via Specific Energy Loss in the TPC

The TPC data, that was created in the simulation, can be used to reconstruct the particles over the differential energy loss dE/dx. Therefore, we want to fit a Bethe-Bloch function on the data, which will give us the particle mass and eventually the particle ID.

7.1.1 ALEPH External Parametrization

Based on this, we can now plot the differential energy loss against the momentum of the particle, and the Bethe-Bloch function is fitted with a multifit onto all curves. More specifically, the ALEPH External parametrization as a function of $\beta\gamma$ which was introduced by Blum and Rolandi for the ALEPH experiment [32]. To derive the parametrization, we first have a look at the Bethe-Bloch equation:

$$-\left[\frac{dE}{dx}\right] = \frac{4\pi N e^4}{m_e^2}\frac{z^2}{\beta^2}\left[\frac{1}{2}\ln\left(\frac{2m_e c^2 E_{max}\beta^2\gamma^2}{I^2}\right) - \frac{\beta^2}{2} - \frac{\delta(\beta)}{2}\right]. \tag{39}$$

With introduction of the free parameters and the neglection of the density term with $\delta(\beta) = 0$ we get

$$\begin{aligned} a_0 &= \frac{2\pi N e^4}{m_e c^2} z^2 \\ a_1 &= \ln\left(\frac{2m_e c^2 E_{max}}{I^2}\right) \rightarrow e^{a_1} = \frac{2m_e c^2 E_{max}}{I^2}. \end{aligned} \tag{40}$$

We can transform the equation to

$$-\left[\frac{dE}{dx}\right](\beta\gamma; a_0, a_1) = \frac{a_0}{\beta^2}\left[\ln\left(e^{a_1}\beta^2\gamma^2\right) - \beta^2\right] \tag{41}$$

by using $\ln(\frac{a}{b}) = \ln(a) - \ln(b)$ it follows, that

$$-\left[\frac{dE}{dx}\right](\beta\gamma; a_0, a_1) = \frac{a_0}{\beta^2}\left[a_1 - \ln\left(\frac{1}{\beta^2\gamma^2}\right) - \beta^2\right]. \tag{42}$$

Until this point, we neglected the term $\delta(\beta)$. This can be compensated by a free parameter a_2 in the logarithmic term, which gives us the plateau at high momenta :

$$-\left[\frac{dE}{dx}\right](\beta\gamma; a_0, a_1) = \frac{a_0}{\beta^2}\left[a_1 - \ln\left(a_2 + \frac{1}{\beta^2\gamma^2}\right) - \beta^2\right]. \tag{43}$$

The quadratic decrease of the average differential energy loss at low momenta ($\beta\gamma$ <1) and the logarithmic rise at high momenta can be described by the free parameters a_3 and a_4, which can

be assumed to be $a_3, a_4 \approx 2$ by looking at the Bethe-Bloch formula, we get the expression for the ALEPH-External parametrization

$$-\left[\frac{dE}{dx}\right]_{\text{ALEPH External}}(\beta\gamma; a_0, a_1) = \frac{a_0}{\beta^{a_3}}\left[a_1 - \ln\left(a_2 + \frac{1}{(\beta\gamma)^{a_4}}\right) - \beta^{a_3}\right] \tag{44}$$

which was used for the fits of the average differential energy plot against the momentum [32].

7.1.2 Classification

In Fig. 42, the ALEPH fits on the curves of the different particles are shown.

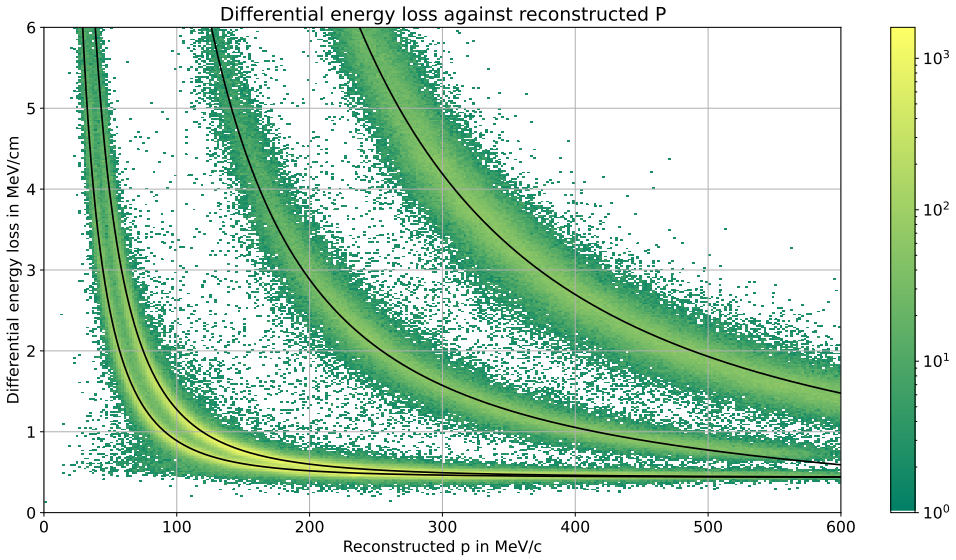

Figure 42: Differential energy loss plot against the momentum and in black the ALEPH fits

On every of those fits, an error band of the deviation of the data can be calculated as shown for protons in Fig. 43

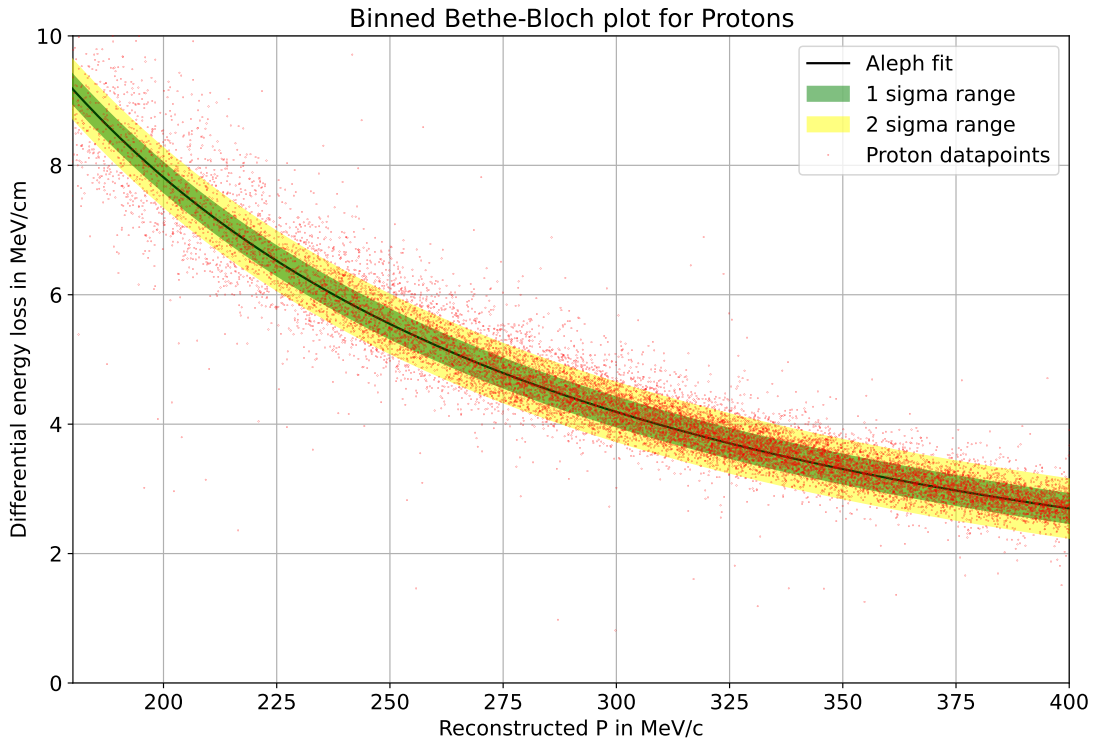

Figure 43: ALEPH fit with Error band for protons. A binned fit was performed, meaning, that the initial data points were binned in bins with a width of 10 MeV/c. On those bins a Gaussian was fitted. The mean and standard deviation of the Gaussian were then used as the data points for the fit.

This means every data point has now a certain sigma deviation to the different ALEPH fits, which all correspond to either a proton, kaon, pion or muon. To perform a PID on one of those particles, the sigma deviation to all of those curves is calculated, and the lowest deviation gives us the particle's ID.

$$\text{PID}(\text{particle}) = \underset{\forall p \in \chi}{\text{argmin}} \left\{ \frac{\text{dist}(\text{particle}, \text{ALEPH}_\text{p})}{\sigma_p} \right\} \tag{45}$$

where χ is the set of all possible particles (proton, kaon, pion and muon).
Lastly, one can see an overlap in Fit. 42 of the two lowest curves, being the pions and muons, as they have similar masses. This will lead to a significant error in PID, as there's no distinctiveness in their energy loss at higher momenta. This however is solved, as we only want to look at primary particles directly emerging from the collision, which will cut out all muons falsely identified as pions, because they only appear as secondary particles from decays.

7.2 PID with ML Framework

Besides the Bethe-Bloch PID, we will also use a Machine Learning classifier. It should be mentioned, that again the DCA primary cut was used, to only have primary protons, kaons, pions and secondary muons in the dataset. The model of choice is a Boosted Decision Tree (BDT), which was explained in more detail in Chapter 4. To use this model, some parameters still need to be set. On one hand, we need a feature vector of the physical data, we want to use with a corresponding label, being the particle identity. On the other hand, we will need to fix some hyperparameters regarding the decision trees, which will be explained in the following part.

7.2.1 Feature Vector

Feature	Unit	Reconstruction
Transverse momentum p_T	MeV/c	Circle fit
χ^2 of p_T	-	Circle fit
z-momentum p_z	MeV/c	Helix fit
Momentum p	MeV/c	comb. of p_T and p_z
χ^2 of p	-	From Helix fit
differential Energy loss dE/dx	MeV/cm	energy deposition and hit position
average distance between hits dx	cm	from hit positions
Number of TPC hits	-	direct output
charge Q	-1,1	helix orientation
Daughter muon momentum	MeV/c	comb. of p_T and p_z
Daughter muon transverse momentum	MeV/c	Circle fit
Number of daughters	-	True value

Table 8: List of used features for the ML framework

For the feature vector used in the ML framework, shown in Tab. 8, nearly all reconstructed or measured values were used, that could be compromised into a single scalar value. An interesting choice to mention are the momenta of possible daughter muons of a particle. This selection of those features will be more clear with the explanation of Chapter 7.3, as it shows, that the momenta of the daughter muons in combination with the initial momentum show a great separability between kaons and pions. As no full track reconstruction was done, the connection of the daughter to the parent particle and the number of daughters are used from the true values.

7.2.2 Hyperparameter Tuning

The goal of hyperparameter tuning is to find the optimal set of hyperparameters with which to train our classifier. To find good parameters, we need to define our set of hyperparameters

and what good means. Therefore, we will use the measure of accuracy defined as:

$$\text{Accuracy} = \frac{\text{TP} + \text{TN}}{\text{TP} + \text{TN} + \text{FP} + \text{FN}} \tag{46}$$

with TP (true positive) and TN (true negative) the number of correctly predicted classes and FP (false positive) and FN (false negative) the incorrectly predicted classes. The set of adjustable hyperparameters can be seen in Tab. 9.

Hyperparameter	optimization range
`learning_rate`	0.01–0.3
`max_depth`	3–9
`n_estimators`	100–500
`gamma`	0.1–1
`lambda`	0.1–1
`alpha`	0.1–1

Table 9: Hyperparameters of used BDT

where the `learning_rate` gives us the step size of the optimization, `max_depth` the maximum depth of a tree, `n_estimators` the number of boosting rounds/trees, `gamma` the minimum loss that is required to make a further partition of a node, `lambda` the L2 regularization scaling and `alpha` the L1 regularization scaling.
Optuna's optimization [33] was performed to maximize the accuracy score with a total of 200 trials. During each iteration, a new classifier is trained, and a 5-fold cross validation was done, where the dataset is partitioned into 5 parts, where 4 parts are used for training and 1 part for testing. After optimization, the classifier reached an accuracy of 0.9898 with the parameter values depicted in Tab. 10.

Hyperparameter	Best value
`learning_rate`	0.11
`max_depth`	4
`n_estimators`	294
`gamma`	0.11
`lambda`	0.50
`alpha`	0.146

Table 10: Values of Optuna optimized hyperparameters

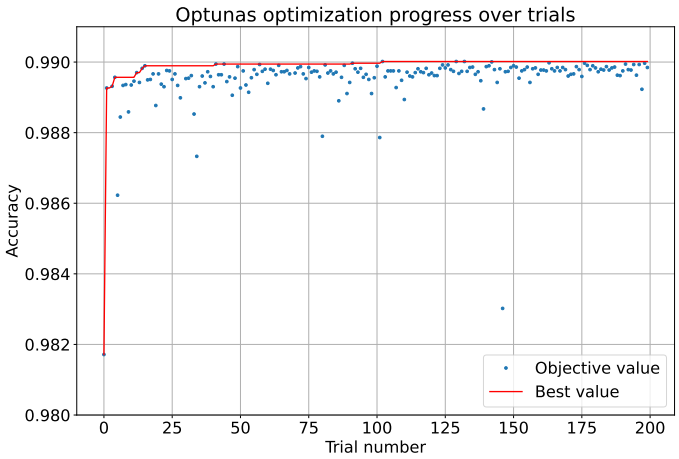

Figure 44: Optimization history of Optuna parameter optimization.

7.2.3 Framework Analysis

Before comparing the performance of the ML framework and the Bethe-Bloch PID, one can have a closer look at the ML performance to have a first insight of its capabilities and analyse the structure with regard to the generality, separability, and feature importance.

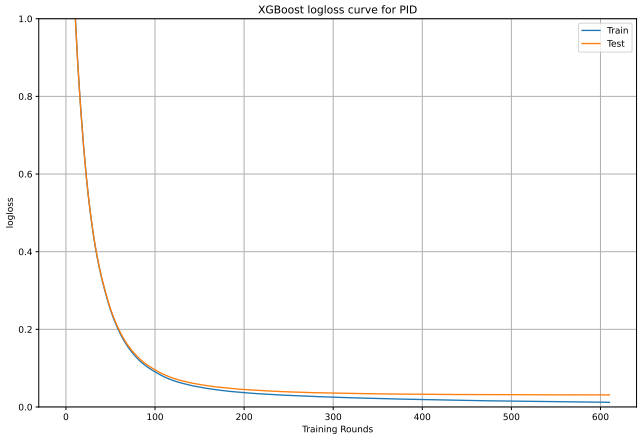

Figure 45: Logloss of the BDT over the training rounds.

The logloss plot in Fig. 45 reveals a sharp decline in logarithmic loss during the initial training rounds, followed by a flattening of both curves as training progresses, indicating effective model optimization. The small difference between the training and test set curves suggests that the BDT model generalizes well without signs of overfitting.

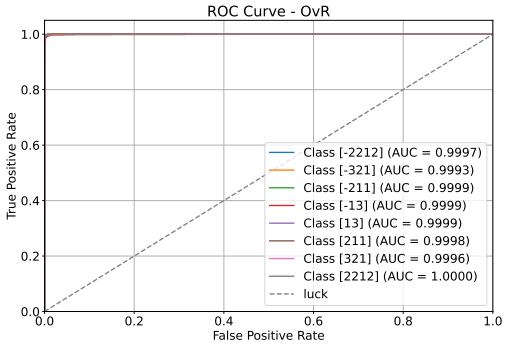

Figure 46: ROC curve OvR of the different particle classifications.

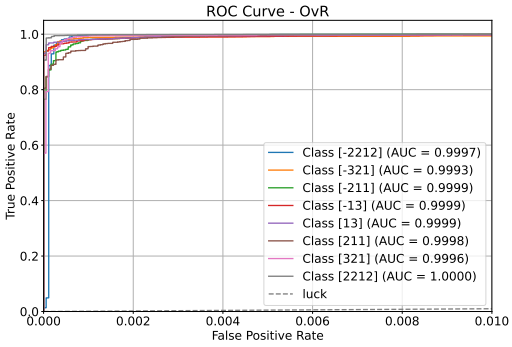

Figure 47: Zoomed in ROC curve OvR of the different particle classifications.

The ROC (Receiver Operating Characteristic) curve is a graphical representation that plots the True Positive Rate (TPR) against the False Positive Rate (FPR). The TPR and FPR are calculated by

$$\begin{aligned} \text{TPR} &= \frac{\text{TP}}{\text{TP} + \text{FN}} \\ \text{FPR} &= \frac{\text{FP}}{\text{FP} + \text{TN}} \end{aligned} \tag{47}$$

where TP represents the number of true positives, FN the number of false negatives, FP the number of false positives, and TN the number of true negatives. As we have a multiple classes and not only two, we look at the One vs Rest (OVR) ROC, where one class is represents the signal and all others the background. The area under the ROC curve (AUC) serves as a key metric for evaluating the performance of a classifier. An ideal classifier will have an AUC of 1.0, indicating perfect performance. As illustrated in Fig. 47, the ROC curve closely aligns with that of a perfect classifier, with only a minimal deviation. This is further supported by the AUC score, which is close to 1, indicating an almost perfect separation between the classes.

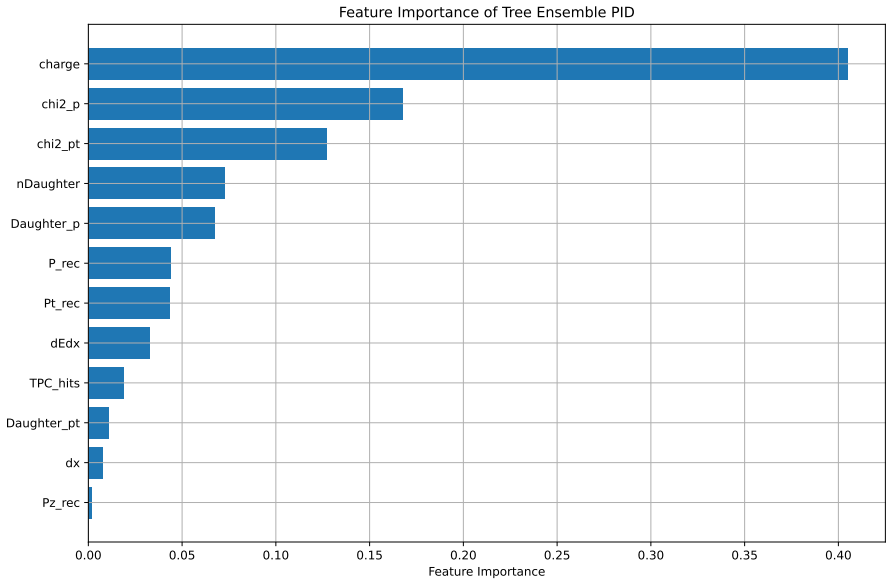

Figure 48: Feature importance of the BDT.

In XGBoost, feature importance based on gain represents the average improvement in the model's accuracy when a feature is used to split the data across all the decision trees. The feature importance is then the average gain as defined in Eq. 25 from all the splits that use that feature, making it a powerful metric for understanding which features contribute the most to improving the model's performance. Features with higher gain scores are more impactful in reducing prediction error, indicating they play a more significant role in the model's decision-making process.

As observed, the charge of the particles, with a feature importance of approximately 0.39, stands out as the most significant factor when considering distance. This is expected, given that for every charged particle, the corresponding antiparticle is also injected, which shares most of its properties except for the charge. This makes the charge feature the primary distinction between a particle and its antiparticle.

More interestingly, the χ^2 values of the momentum reconstructions emerge as crucial, ranking as the second and third most important features, with importances of 0.157 and 0.151, respectively. This observation aligns with other analyses, as different particle species — namely protons, kaons, pions, and muons — experience distinct combinations of physical phenomena like multiple scattering and energy loss. These lead to varying orders of error, potentially resulting in distinctive structures within their χ^2 distributions, which are directly tied to the reconstruction process.

The feature `nDaughter`, which refers to the number of daughter particles, has a feature importance of 0.07. Since different particles undergo different decays and exhibit varying branching ratios, some of these decays can be distinguished by the number of decay products, contributing

to the feature's significance.
Additionally, the momentum of a possible daughter muon, `Daughter_p`, plays a notable role. The very existence of a daughter particle can introduce a distinguishing feature. Furthermore, the combination of the daughter muon's momentum with the primary particle's momentum, `P_rec`, which follows with a feature importance of 0.045, helps distinguish between kaons and pions particularly well, as explained in more detail in the subsequent chapter.
The transverse momentum, `Pt_rec`, holds a feature importance of approximately 0.043, which is on par with the total reconstructed momentum, `P_rec`. Both of these features are relatively important because the simulated momentum ranges for the different particles vary, contributing to the differentiation.
Interestingly, the differential energy loss, `dEdx`, exhibits a lower feature importance of 0.034, despite being one of the main properties used for PID via the Bethe-Bloch formula.
Lastly, features such as the number of TPC hits (`TPC_hits`), the transverse momentum of the possible daughter muon (`Daughter_pt`), the average hit distance in the TPC (`dx`), and the z-component of the primary particle's momentum (`Pz_rec`) seem to have relatively low importance. This could be because these values are either similar across all particles in the simulation setup or highly correlated with other features, such as `Daughter_p`, `P_rec`, and `Pt_rec`, thereby not providing much additional information.

7.3 PID of Pions and Kaons via Secondary Muon Momenta

To classify the primary particles, which do not reach the TPC, one needs to find a distinguishing feature in their decays, as they do not reach far enough into the detector to classify them directly. For kaons and pions, it seems plausible to look at the muon momenta of the decays, as nearly all pions decay into muons (Chap. 1.4.3) and over 60 of the kaons (Chap. 1.4.2). Moreover, the masses of kaons and pions are very different, which should lead to a mayor difference in the momentum of the muons. To calculate the resulting muon momenta, one needs to take the invariant masses of the initial and final state of the $K^-/\pi^- \to \mu^-\bar{\nu}_\mu$ decay or their respective antiparticle decays.

$$\begin{aligned} P_\pi^2 &= P_{\mu\nu}^2 \\ \Leftrightarrow \begin{pmatrix} E_\pi^2 \\ 0 \end{pmatrix} &= \begin{pmatrix} E_\mu + E_\nu \\ 0 \end{pmatrix}^2 \end{aligned} \tag{48}$$

As this is a two body decay, we have $\bar{P}_m u = -\bar{P}_n u$. Moreover, we assume the antineutrino to be massless, which leads to $E_\nu = |\bar{P}_\nu|$.

$$\begin{aligned}
&\Leftrightarrow m_\pi^2 = (E_\mu + |\bar{P}_\mu|)^2 \\
&\Leftrightarrow m_\pi = E_\mu + |\bar{P}_\mu| \\
&\Leftrightarrow (m_\pi - |\bar{P}_\mu|)^2 = E_\mu^2 \\
&\Leftrightarrow m_\pi^2 - 2m_\pi|\bar{P}_\mu| + |\bar{P}_\mu|^2 = m_\mu^2 + |\bar{P}_\mu|^2 \\
&\Leftrightarrow \frac{m_\pi^2 - m_\mu^2}{2m_\pi} = |\bar{P}_\mu|
\end{aligned} \tag{49}$$

For the pion, we get a muon momentum of $|\bar{P}_\mu(\pi)| \approx 29.79\text{MeV}/c$ and for the kaon $|\bar{P}_\mu(K)| \approx 235.53\text{MeV}/c$. This result seems to be promising already, but this is still in the rest frame of the pion/kaon, but we need the momenta in the rest frame of the detector. This means the muon momenta need to be boosted according to the momentum and the decay angle of the primary particle.

$$u = \frac{\sqrt{u'^2 + v^2 + 2vu'\cos(\theta') - \left(\frac{vu'\sin(\theta')}{c}\right)^2}}{1 + \frac{v}{c^2}u'\cos(\theta')} \tag{50}$$

Where u' is the initial velocity of the primary particle, v the velocity of the decay-muon in the rest frame of the primary particle and θ' the decay angle in the rest frame [34]. Lastly we need to convert the momenta into velocities with

$$v = \frac{|\bar{P}|}{\sqrt{E^2 \cdot |\bar{P}|^2}} \tag{51}$$

and after the boost back into the momentum

$$|\bar{P}| = \beta\gamma m \tag{52}$$

Now we have the momentum of the muons from the decay of the kaons and pions respective to their initial momentum.

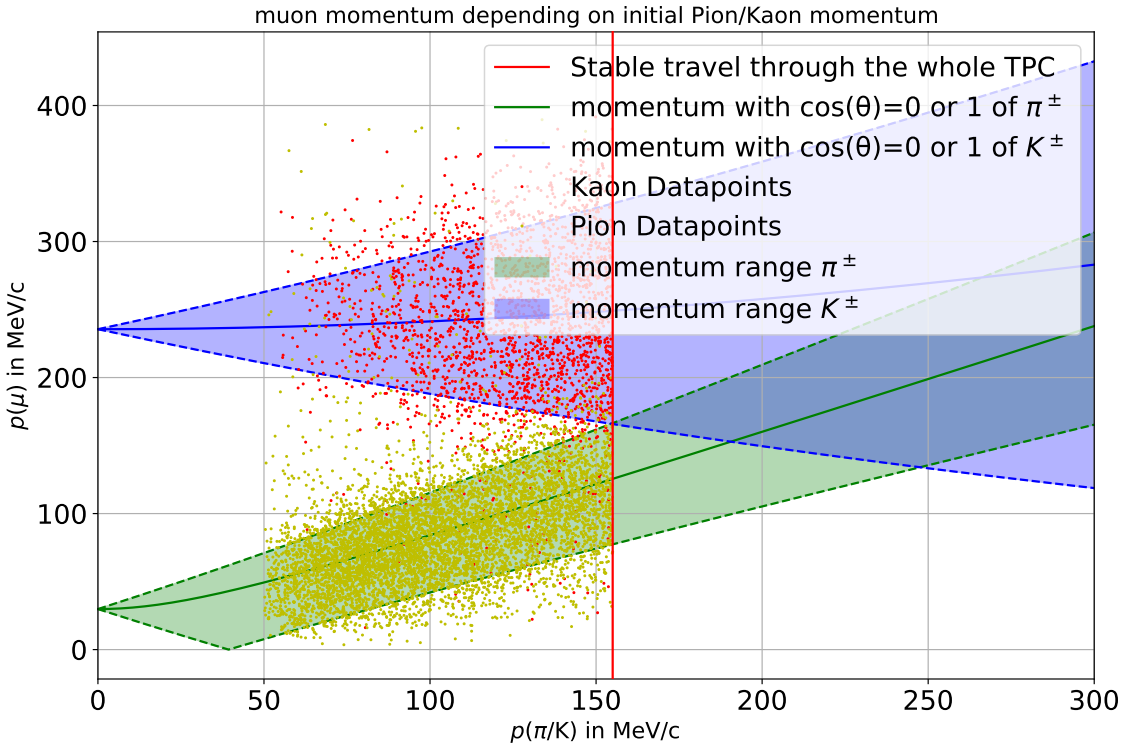

Figure 49: muon momenta respective to the initial primary particle momentum

In Fig. 49, the muon momentum is plotted against the initial primary particle momentum in dependence of the decay angle. One can see, that especially in the low momentum regime, the overlap is minimal or non-existent. As for the higher momenta above ≈160 MeV/c the muon momenta overlap, but from this point on the velocity of the kaons and pions are large enough to travel stable through the whole TPC before decaying, so the primary particles themselves can be reconstructed normally without the investigation of the muon momenta. This means, that the reconstruction via the decay-muons may be a viable way to classify the pions and kaons, by assigning the particle ID, if the momenta lie within the range for charged pions or kaons in Fig. 49.

8 Analysis of PID

Before starting the analysis, another significant cut to the data was made for the PID. As already stated, the primary objective of the low momentum observation is to look at the capability of reconstructing particles directly emerging from the collision. This means in the PID we will only look at primary protons, kaons, pions and secondary muons, reconstructed by the DCA (Chap. 5.5) primary cut.
As for the analysis itself, we will look at two different things, Firstly the comparison between the performance of the models and secondly what the performance of the models tells us about the physical limitations ins terms of the lower momentum limit border.

8.1 Purity and Effiency

Before we can perform the analysis, the parameters with which we perform it must be specified. Therefore, two different indicators are used, the purity and the efficiency of the PID defined as following:

$$P = \frac{N_S}{N_S + N_B} \tag{53}$$

$$E = \frac{\#\text{ of correctly classified particles of species}}{\#\text{ of all simulated particles of species}} \tag{54}$$

This means, the purity gives us a measure, of what ratio of classified particles of for example pions are actually pions and not falsely classified as such. The efficiency shows, how many of the classifiable particles of a species were actually classified as such.

8.2 Purity and Efficiency of Bethe-Bloch and ML PID

In the following plots, one can see the purities and efficiencies of the proton PID for the Bethe-Bloch classification and the ML classification for different transverse momenta. In green, the line of the current momentum limit is depicted.

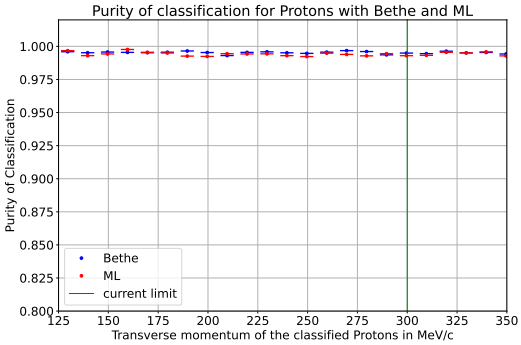

Figure 50: Purity of proton PID via Bethe and ML

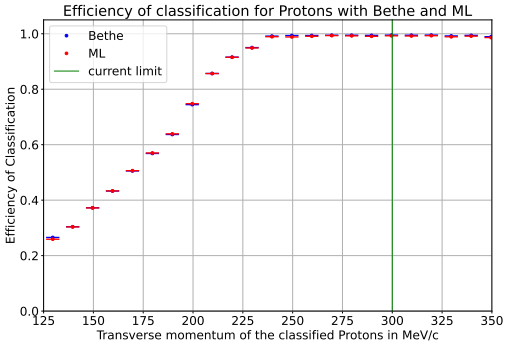

Figure 51: Efficiency of proton PID via Bethe and ML

In Fig. 50 and 51, the performance of the proton PID is shown. As one can see, the purities and efficiencies for both ML and Bethe-Bloch are very similar to each other, which was already expected. As the proton is the only stable particle and has a significantly higher mass than the other particles, a Bethe-Bloch classification is more than sufficient to classify protons as such. This means, there is not much room for improvement with a ML framework, hence the similar results.
However, the efficiency shows an interesting development to the lower momentum regime. From around 230 MeV/c on, the efficiency of both classifications is steadily decreasing. This is due to the energy loss the high mass protons are experiencing, as they begin to stop before even reaching the TPC, which is needed for the energy deposition measurements. Yet, the efficiency is high enough, well below the current limit.

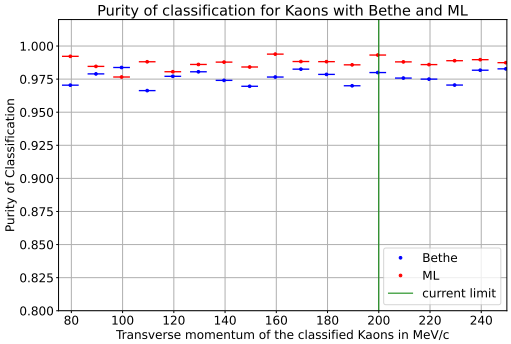

Figure 52: Purity of kaons PID via Bethe-Bloch and ML

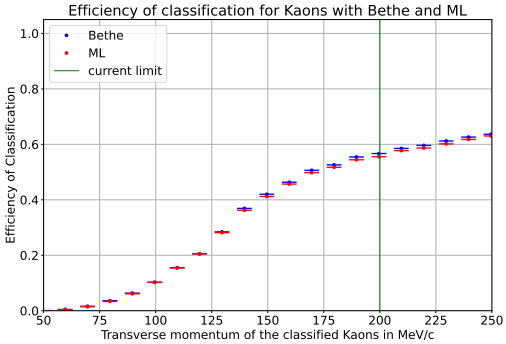

Figure 53: Efficiency of kaons PID via Bethe-Bloch and ML

The PID for kaons, shown in Fig. 52 and 53, behaves very similar to the classification of protons, as kaons, too, have a big mass gap around them, which makes the Bethe classification very precise, which again shows in the similarity of the classification methods.
The efficiency has a similar shape to the proton curve, but the curve is overall much lower. This is due to the problem, that the kaon has two restrictions, that prevent it from reaching the TPC. On the one hand, the energy loss from traversing the inner detector layers is still very significant, as the mass from the kaon is relatively high. On the other hand, the kaon is an unstable particle which means, that particles do not need to be completely stopped like the protons, but the energy loss decreases the decay length. Therefore, the kaon has the lowest classification efficiency overall, as it's the highest mass unstable particle in the context of the thesis.
Still, the efficiency stays reasonably high way past the 200 MeV/c threshold.

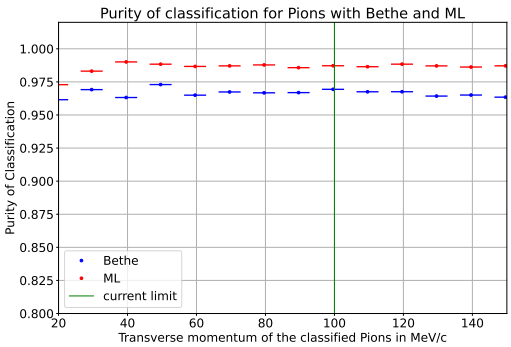

Figure 54: Purity of pions PID via Bethe-Bloch and ML

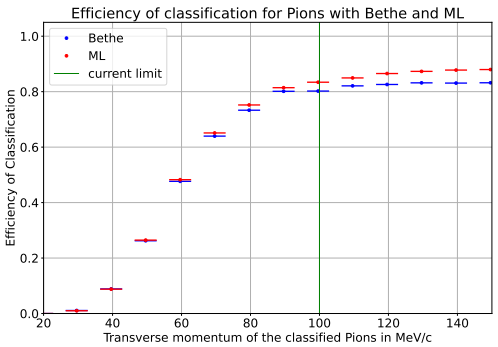

Figure 55: Efficiency of pions PID via Bethe-Bloch and ML

When moving on to particles, that lie within close mass range with another particle, the Bethe-Bloch PID starts to have its problems. In Fig. 54 and 55, a slight difference in performance between the Bethe-Bloch and ML PID is visible. Especially the performance difference in the efficiency is interesting, as it show a clear momentum dependence, with a widening gap between the ML framework and the Bethe-Bloch classification.

At the beginning of the section, it was explained, that we only look at primary protons, kaons and pions and secondary muons for the PID analysis and that is, where the differences in the methods lie. Even though we only look at primary pions, those can still be misidentified as muons and then be cut out of the muon PID, as they are primaries. The ML framework also shows its capabilities in separating those higher momentum pions and muons, which explains the widening gap, as the Bethe-Bloch curves get closer with higher momenta, resulting in a greater overlap, leading to more misclassification which need to be cut out. As the DCA primary cut is not 100 % pure, this also lowers the purity of the classification.

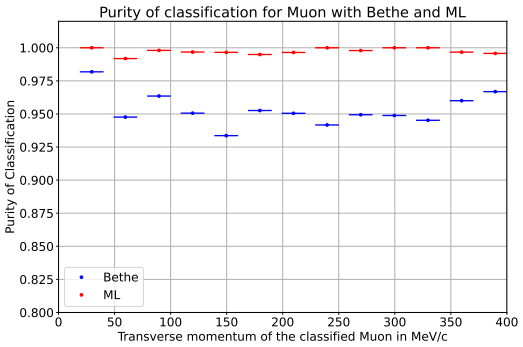

Figure 56: Purity of muon PID via Bethe-Bloch and ML

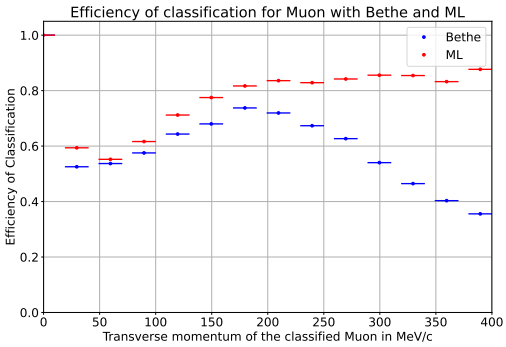

Figure 57: Efficiency of muon PID via Bethe and ML

Lastly, we look at the purity and efficiency of the muon PID in Fig. 56 and 57. The muon PID has a similar structure to the pion PID, as they are the ones overlapping, causing the same

problems as for the pion. However, there is a clear difference in the size of the gap between the efficiencies. This can be explained by the fact that the sigma bandwidth of the ALEPH fits is larger for the pions, which results in a larger number of misclassified muons, which are ultimately missing in the Bethe-Bloch PID for muons.

8.3 Purity and Efficiency of PID via Decay Muons

In the following plots, the purities and efficiencies of the kaon and pion PID with the decay muon classification are shown at different transverse momenta. The green line indicates the current momentum limit.

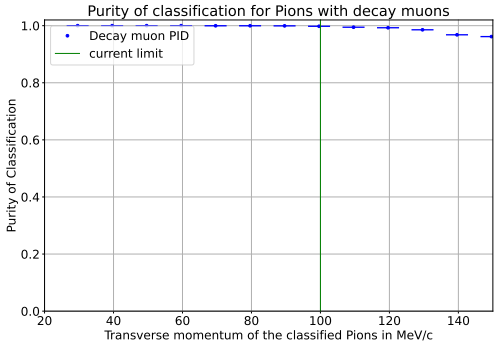

Figure 58: Purity of pions PID with decay muons

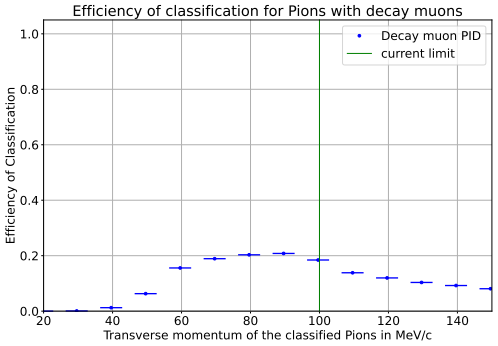

Figure 59: Efficiency of pions PID with decay muons

As shown in Fig 60, the purity of the PID for pions exhibits minimal imperfections, suggesting that separating kaons from pions based on the momentum of their decay muons is feasible. However, the efficiency is notably low, with no improvement in the low momentum regions compared to the standalone TPC PIDs utilizing the Bethe-Bloch and ML frameworks (Fig. 61). This inefficiency is attributed to insufficient momentum reconstruction by the ITS2, particularly in the low momentum region, as shown in Fig. 49. In this region, small errors can cause particles to fall outside the classification range for pions.

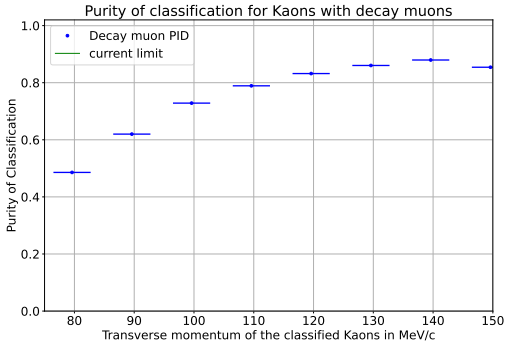

Figure 60: Purity of kaons PID with decay muons

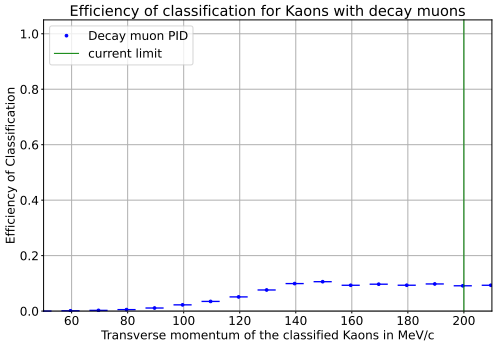

Figure 61: Efficiency of kaons PID with decay muons

For kaons, separability from pions presents some challenges, remaining below 90%, with a sharp decline in the lower momentum regions. This decline can be attributed to the decreasing efficiency, as fewer kaons are able to traverse enough ITS2 layers due to significant energy loss. In contrast, the much lighter pions can still pass through these layers at the same momentum, resulting in a higher ratio of misclassified pions. This issue is further exacerbated by the poor ITS2 momentum resolution at low momenta, as shown in Fig. 22.
Overall, the PID via decay muons of pions and kaons faces expected challenges due to insufficient momentum reconstruction by the ITS2 at low momenta. However, it still demonstrates promising results in terms of purity for pions. This suggests that, with a more advanced momentum reconstruction achieving a resolution closer to Fig. 6, there is potential for significant performance improvement, making this a viable PID method for pions and kaons in the low momentum regions.

9 Summary and Outlook

The primary goal of this thesis was to explore the limitations of tracking and PID for protons, kaons, and pions at low transverse momenta in ALICE Run 3, as measurements in this regime could validate several interesting theoretical predictions [2]. To this end, a simplified standalone Geant4 simulation of the innermost detectors was performed [25]. This allowed the reconstruction of particle properties, providing insights into potential challenges and limitations in tracking and PID in this momentum range.

In terms of track reconstruction, momentum measurements using the ITS2 exhibited high uncertainties in the low momentum regime (Figs. 20, 21, 22), primarily due to significant multiple scattering in the ITS layers. This indicates that the conventional approach detailed in Chapter 7 may not be feasible at these low momenta. However, the prominent scattering could provide an opportunity to explore momentum reconstruction based on the scattering angle between layers. Previous studies have demonstrated promising results in higher momentum regimes using this method [35, 36].
In contrast, TPC-based momentum reconstruction produced significantly better resolution compared to ITS, particularly below the Run 2 limits [1] (Figs. 27, 28, 29). These errors could be further minimized by correcting for energy loss, the primary source of uncertainty.
Moreover, the standalone TPC reconstructions of key quantities, such as the primary vertex (Figs. 32–37), charge (Figs. 38–41), and differential energy loss (Fig. 42), performed well, yielding minimal impurities and a precise Bethe-Bloch plot.
Overall, the track reconstruction results are promising, particularly for standalone TPC reconstructions, which demonstrated high efficiency and accuracy, extending well below the limits observed in Run 2. These reconstructions lay a solid foundation for PID using the Bethe-Bloch method and a ML framework.

In terms of PID, both the Bethe-Bloch method and the ML framework performed favourably. For protons, the ML framework maintained high purity across the entire simulated momentum range, with efficiency only decreasing significantly below 300 MeV/c. The ML framework outperformed the Bethe-Bloch approach for kaons and pions, especially in terms of purity over all simulated momenta. Additionally, kaon and pion PID efficiencies remained high, even below the 200 MeV/c and 100 MeV/c thresholds, respectively.

In conclusion, the results indicate that low-p_T reconstruction for protons, kaons, and pions may be feasible in ALICE Run 3. The ML framework appears to be a valuable complement, likely to improve further with the inclusion of real background data. While these results are encouraging, they should be taken with a grain of salt due to the simplifications made in this initial study, which served as an exploratory investigation into previously uncharted momentum

regions in Run 3.

The next logical step would be to develop a more sophisticated simulation with realistic detector geometries and full collision generation, more complex and complete reconstruction and PID methods, such as a Kalman filter for tracking and ITS2-TPC matching. This will allow further validation of these findings and guide efforts toward reconstructing data from ALICE Run 3. Additionally, improving ITS2-based momentum reconstruction could enhance kaon and pion PID, particularly in distinguishing these particles from decay muons at lower momenta, unveiling insights into even lower momenta.

List of Figures

List of Tables

References

[1] S. Acharya et al. "Production of charged pions, kaons, and (anti-)protons in Pb-Pb and inelastic pp collisions at sNN = 5.02 TeV". In: *Physical Review C* 101.4 (Apr. 2020). ISSN: 2469-9993. DOI: 10.1103/physrevc.101.044907. URL: http://dx.doi.org/10.1103/PhysRevC.101.044907.

[2] B. Mohanty and J. Serreau. "Disoriented chiral condensate: Theory and experiment". In: *Physics Reports* 414.6 (Aug. 2005), pp. 263–358. ISSN: 0370-1573. DOI: 10.1016/j.physrep.2005.04.004. URL: http://dx.doi.org/10.1016/j.physrep.2005.04.004.

[3] Viktor Begun and Wojciech Florkowski. "Bose-Einstein condensation of pions in heavy-ion collisions at energies available at the CERN Large Hadron Collider". In: *Physical Review C* 91.5 (May 2015). ISSN: 1089-490X. DOI: 10.1103/physrevc.91.054909. URL: http://dx.doi.org/10.1103/PhysRevC.91.054909.

[4] B. B. Back et al. "Particle production at very low transverse momenta in Au+Au Collisions at s(NN)**1/2 = 200 GeV". In: *Physical Review C* 70.5 (Nov. 2004). ISSN: 1089-490X. DOI: 10.1103/physrevc.70.051901. URL: http://dx.doi.org/10.1103/PhysRevC.70.051901.

[5] B Abelev et al and (The ALICE Collaboration). "Technical Design Report for the Upgrade of the ALICE Inner Tracking System". In: *Journal of Physics G: Nuclear and Particle Physics* 41.8 (July 2014), p. 087002. DOI: 10.1088/0954-3899/41/8/087002. URL: https://dx.doi.org/10.1088/0954-3899/41/8/087002.

[6] Mark Thomson. *Modern Particle Physics*. Cambridge University Press, 2013.

[7] Matic Lubej. *Standard Model*. URL: https://www.physik.uzh.ch/groups/serra/StandardModel.html.

[8] S. Navas et al. "Review of particle physics". In: *Phys. Rev. D* 110.3 (2024), p. 030001. DOI: 10.1103/PhysRevD.110.030001.

[9] H. Bethe. "Zur Theorie des Durchgangs schneller Korpuskularstrahlen durch Materie". In: *Annalen der Physik* 397.3 (1930), pp. 325–400. DOI: https://doi.org/10.1002/andp.19303970303. eprint: https://onlinelibrary.wiley.com/doi/pdf/10.1002/andp.19303970303. URL: https://onlinelibrary.wiley.com/doi/abs/10.1002/andp.19303970303.

[10] F. Bloch. "Zur Bremsung rasch bewegter Teilchen beim Durchgang durch Materie". In: *Annalen der Physik* 408.3 (1933), pp. 285–320. DOI: https://doi.org/10.1002/andp.19334080303. eprint: https://onlinelibrary.wiley.com/doi/pdf/10.1002/andp.19334080303. URL: https://onlinelibrary.wiley.com/doi/abs/10.1002/andp.19334080303.

[11] Enrico Fermi. "The Ionization Loss of Energy in Gases and in Condensed Materials". In: *Phys. Rev.* 57 (6 Mar. 1940), pp. 485–493. DOI: 10.1103/PhysRev.57.485. URL: https://link.aps.org/doi/10.1103/PhysRev.57.485.

[12] M. Tanabashi et al. "Review of Particle Physics". In: *Phys. Rev. D* 98 (3 Aug. 2018), p. 030001. DOI: 10.1103/PhysRevD.98.030001. URL: https://link.aps.org/doi/10.1103/PhysRevD.98.030001.

[13] M. Tanabashi et al. "Review of Particle Physics". In: *Phys. Rev. D* 98 (3 Aug. 2018), p. 030001. DOI: 10.1103/PhysRevD.98.030001. URL: https://link.aps.org/doi/10.1103/PhysRevD.98.030001.

[14] Virgil L. Highland. "Some practical remarks on multiple scattering". In: *Nuclear Instruments and Methods* 129.2 (1975), pp. 497–499. ISSN: 0029-554X. DOI: https://doi.org/10.1016/0029-554X(75)90743-0. URL: https://www.sciencedirect.com/science/article/pii/0029554X75907430.

[15] J. Wolberg. "Data Analysis Using the Method of Least Squares: Extracting the Most Information from Experiments". In: (Jan. 2006), pp. 1–250. DOI: 10.1007/3-540-31720-1.

[16] E.L. Lehmann and Joseph P. Romano. *Testing Statistical Hypotheses*. Cham: Springer, 2022. ISBN: 978-3-030-70577-0. DOI: 10.1007/978-3-030-70578-7. URL: https://link.springer.com/book/10.1007/978-3-030-70578-7.

[17] The ALICE Collaboration et al. "The ALICE experiment at the CERN LHC". In: *Journal of Instrumentation* 3.08 (Aug. 2008), S08002. DOI: 10.1088/1748-0221/3/08/S08002. URL: https://dx.doi.org/10.1088/1748-0221/3/08/S08002.

[18] "Real-time data processing in the ALICE High Level Trigger at the LHC". In: *Computer Physics Communications* 242 (2019), pp. 25–48. ISSN: 0010-4655. DOI: https://doi.org/10.1016/j.cpc.2019.04.011. URL: https://www.sciencedirect.com/science/article/pii/S0010465519301250.

[19] *ALICE Inner Tracking System (ITS): Technical Design Report*. Technical design report. ALICE. Geneva: CERN, 1999. URL: https://cds.cern.ch/record/391175.

[20] *Upgrade of the ALICE Time Projection Chamber*. Tech. rep. 2013. URL: https://cds.cern.ch/record/1622286.

[21] G Dellacasa et al. *ALICE time projection chamber: Technical Design Report*. Technical design report. ALICE. Geneva: CERN, 2000. URL: https://cds.cern.ch/record/451098.

[22] ALICE Collaboration. *ALICE O2 software*. URL: https://github.com/AliceO2Group/AliceO2.

[23] Ernst Hellbär. *Reconstruction in ALICE and calibration of TPC space-charge distortions in Run 3*. 2021. arXiv: 2109.12000 [physics.ins-det]. URL: https://arxiv.org/abs/2109.12000.

[24] S. Agostinelli et al. "Geant4—a simulation toolkit". In: *Nuclear Instruments and Methods in Physics Research Section A: Accelerators, Spectrometers, Detectors and Associated Equipment* 506.3 (2003), pp. 250–303. ISSN: 0168-9002. DOI: https://doi.org/10.1016/S0168-9002(03)01368-8. URL: https://www.sciencedirect.com/science/article/pii/S0168900203013688.

[25] Andrés Bórquez. *Generation and reconstruction of low pT charged particles (pions, kaons, protons) with no/low magnetic field*. URL: https://github.com/HD-ALICE-Sexaquark/ToyTPC.

[26] Jerome Jungon. "Dielectron Production in pp Collisions at $\sqrt{s} = 13$ TeV Measured in a Dedicated Low Magnetic-Field Setting with ALICE". In: *MDPI Proc.* 10.1 (2019), p. 50. DOI: 10.3390/proceedings2019010050. URL: https://cds.cern.ch/record/2727110.

[27] T.M. Mitchell. *Machine Learning*. McGraw-Hill International Editions. McGraw-Hill, 1997. ISBN: 9780071154673. URL: https://books.google.de/books?id=EoYBngEACAAJ.

[28] T. Chen and C. Guestrin. *XGBoost Introduction to Boosted Trees*. Visited on 10.03.2024. URL: https://xgboost.readthedocs.io/en/stable/tutorials/model.html.

[29] Randy Bullock. *Least-Squares Circle Fit given a finite set of points in R2*. 2017. URL: https://dtcenter.org/sites/default/files/community-code/met/docs/write-ups/circle_fit.pdf.

[30] Purevjav Enkhbayar et al. "HELFIT: Helix fitting by a total least squares method". In: *Computational Biology and Chemistry* 32.4 (2008), pp. 307–310. ISSN: 1476-9271. DOI: https://doi.org/10.1016/j.compbiolchem.2008.03.012. URL: https://www.sciencedirect.com/science/article/pii/S1476927108000418.

[31] D. Antończyk et al. "Performance studies with an ALICE TPC prototype". In: *Nuclear Instruments and Methods in Physics Research Section A: Accelerators, Spectrometers, Detectors and Associated Equipment* 565.2 (2006), pp. 551–560. ISSN: 0168-9002. DOI: https://doi.org/10.1016/j.nima.2006.06.022. URL: https://www.sciencedirect.com/science/article/pii/S0168900206011624.

[32] Walter Blum, Werner Riegler, and Luigi Rolandi. *Particle detection with drift chambers; 2nd ed.* Berlin: Springer, 2008. DOI: 10.1007/978-3-540-76684-1. URL: https://cds.cern.ch/record/1105920.

[33] Takuya Akiba et al. *Optuna: A Next-generation Hyperparameter Optimization Framework*. 2019. arXiv: 1907.10902 [cs.LG]. URL: https://arxiv.org/abs/1907.10902.

[34] John David Jackson. *Classical electrodynamics*. 3rd ed. New York, NY: Wiley, 1999. ISBN: 9780471309321. URL: http://cdsweb.cern.ch/record/490457.

[35] N Agafonova et al. "Momentum measurement by the multiple Coulomb scattering method in the OPERA lead-emulsion target". In: *New Journal of Physics* 14.1 (Jan. 2012), p. 013026. ISSN: 1367-2630. DOI: 10.1088/1367-2630/14/1/013026. URL: http://dx.doi.org/10.1088/1367-2630/14/1/013026.

[36] T Odagawa et al. "Momentum reconstruction of charged particles using multiple Coulomb scatterings in a nuclear emulsion detector". In: *Progress of Theoretical and Experimental Physics* 2022.11 (Oct. 2022), 113H01. ISSN: 2050-3911. DOI: 10.1093/ptep/ptac139. eprint: https://academic.oup.com/ptep/article-pdf/2022/11/113H01/46950089/ptac139.pdf. URL: https://doi.org/10.1093/ptep/ptac139.

Appendix

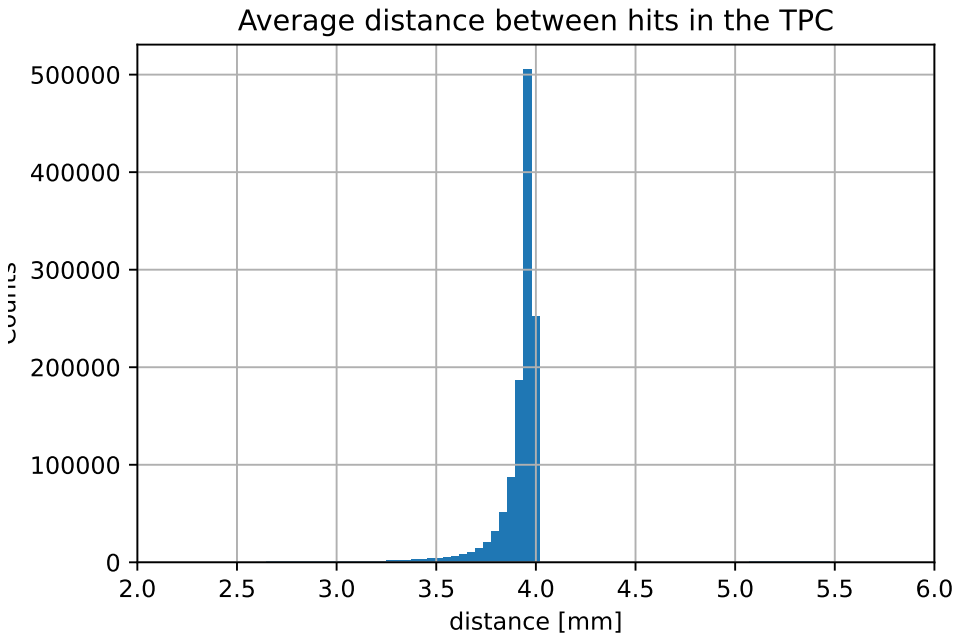

Figure 62: Average hit distances of all particle species in the TPC

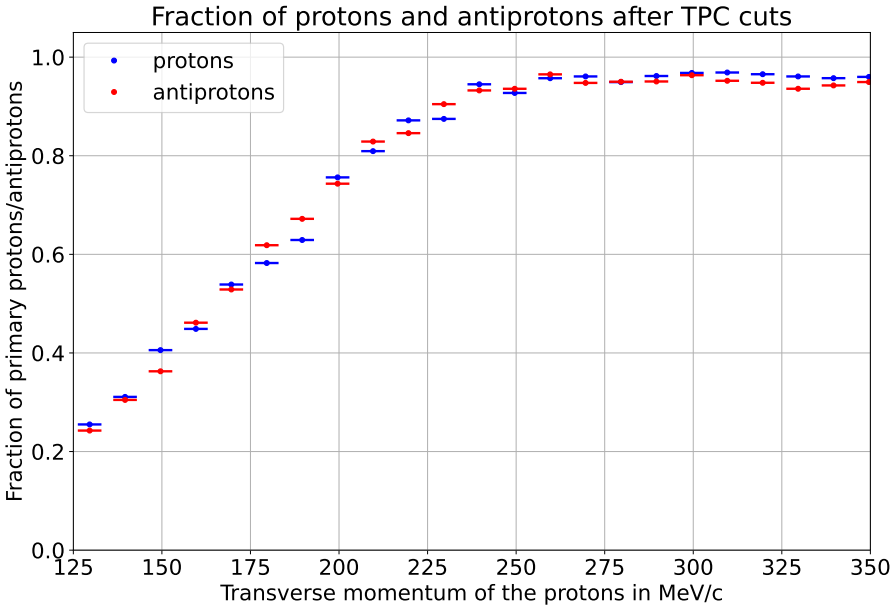

Figure 63: Fraction of primary protons and antiprotons reaching the TPC. As one can see, they are up to statistical fluctuations identical, meaning that a separate analysis is not needed.

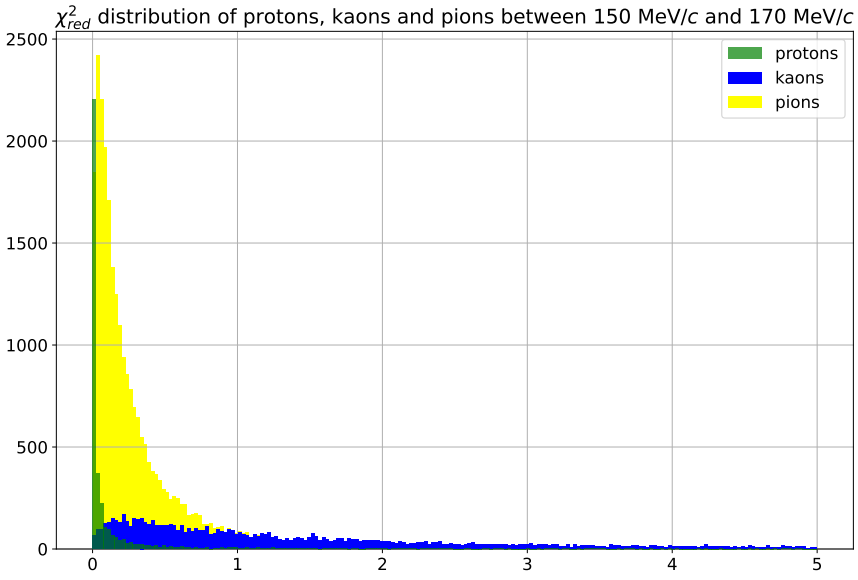

Figure 64: χ^2 distribution of the p_T reconstruction of protons, kaons and pions between an initial transverse momentum of 150–170 MeV/c. One can see the different structures, which leads to the feature importance in the ML framework

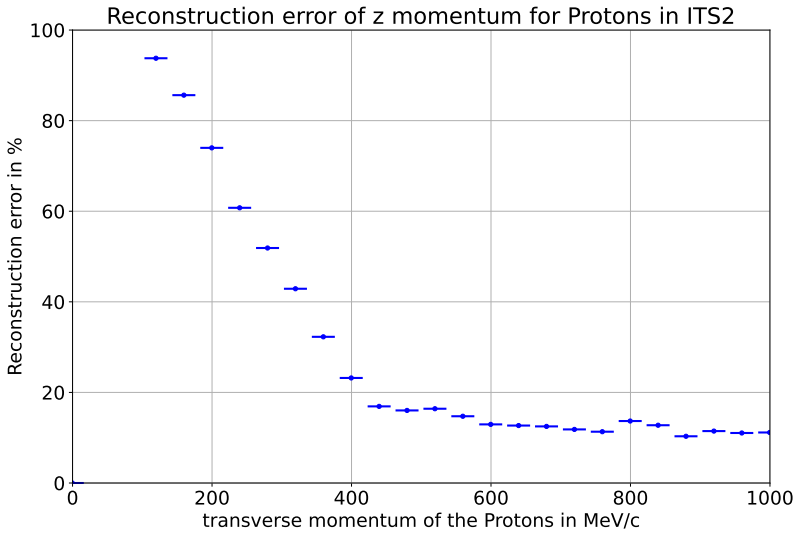

Figure 65: Reconstruction error of the z momentum of standalone ITS2 reconstruction of protons.

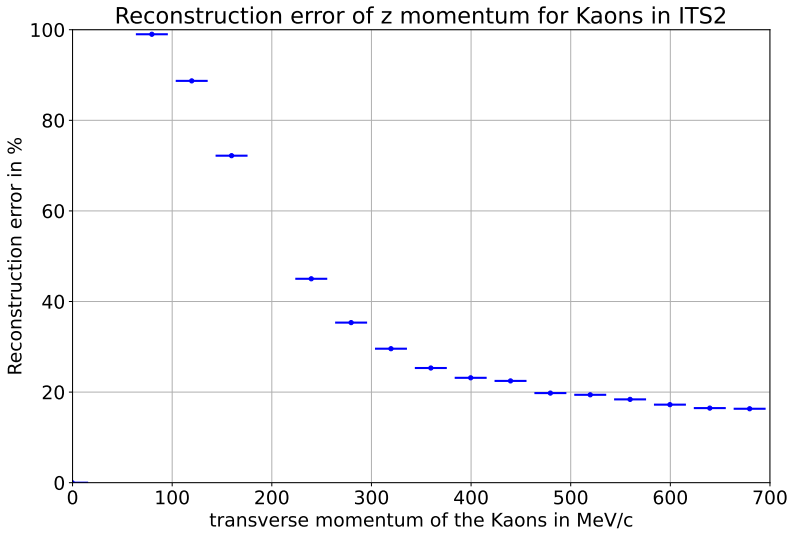

Figure 66: Reconstruction error of the z momentum of standalone ITS2 reconstruction of kaons.

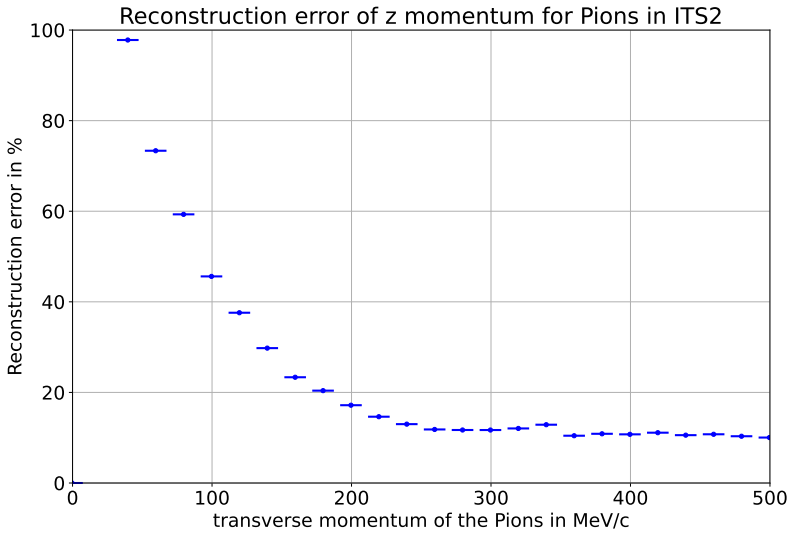

Figure 67: Reconstruction error of the z momentum of standalone ITS2 reconstruction of pions.

In Figs. 65, 66 and 67, the reconstruction errors in the z-momentum are shown. The behaviour is similar to the transverse momentum reconstruction, which is not surprising, as a big part of the z-momentum reconstruction is based on the transverse momentum reconstruction, as we need the circle reconstruction for the helix fit. This means a good transverse momentum reconstruction is directly correlated to a good z-momentum reconstruction.

With the transverse momentum reconstruction from Section 6.2.2, we can now reconstruct the z-momentum, by determining the pitch between the z-momentum and the transverse momentum with a helix fit as given in 5.2 with, as for the circle fit, only the first 70% of the track hits in the TPC are used to account for the late energy loss of the particles.

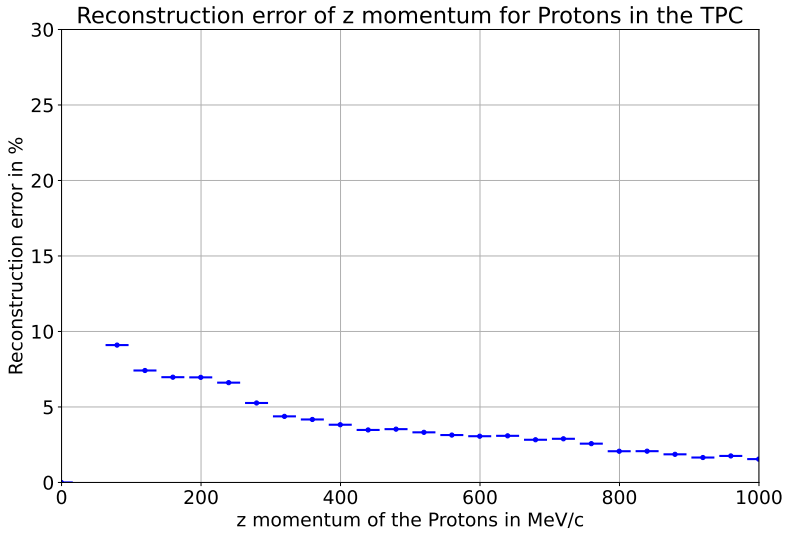

Figure 68: Reconstruction error of the z momentum of standalone TPC reconstruction of protons.

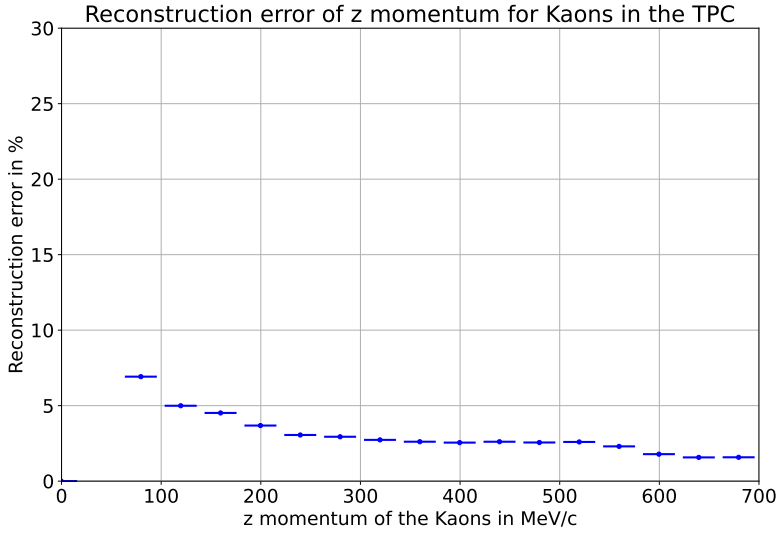

Figure 69: Reconstruction error of the z momentum of standalone TPC reconstruction of kaons.

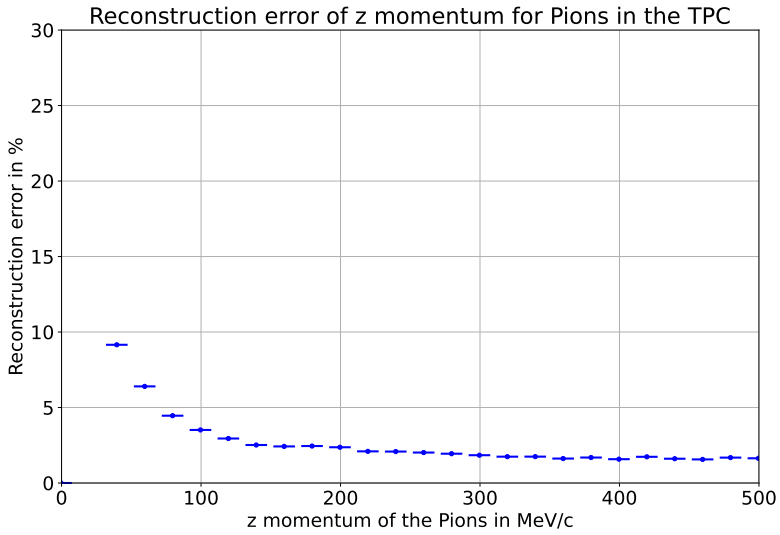

Figure 70: Reconstruction error of the z momentum of standalone TPC reconstruction of pions.

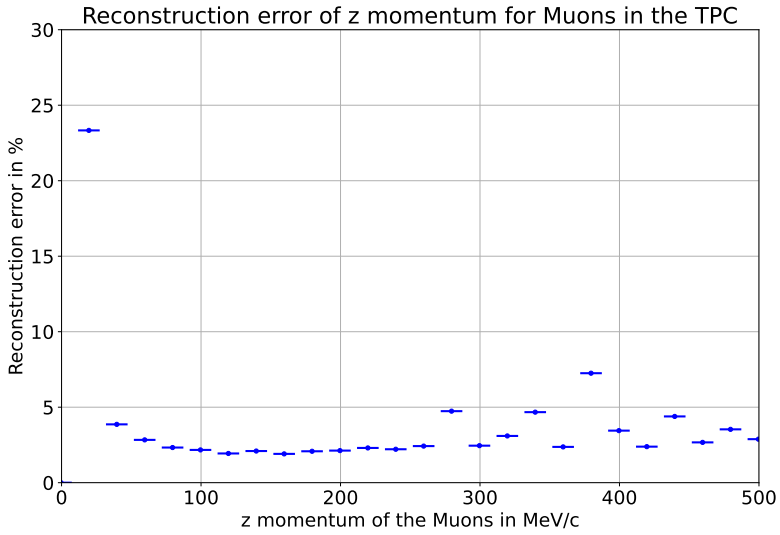

Figure 71: Reconstruction error of the z momentum of Standalone TPC reconstruction of muons

In Figs. 68, 69, 70 and 71, the reconstruction errors in the z-momentum are shown, which is again similar to the ITS reconstruction behaviour, but with a significantly lower error overall. Therefore, the sudden rise in the reconstruction error in the low momentum regime has the same explanation as the rise in the transverse momentum reconstruction, being the energy loss before the TPC.

Acknowledgments

First of all, I want to thank Prof. Dr. Reygers to give me the opportunity to work on such an interesting topic for my Bachelors Thesis and all the help and interesting discussions we had. We had many helpful meetings to talk about the proceedings of the thesis, and he always had an open ear, when problems occurred. I also want to thank him to give me the opportunity to participate in the FSP ALICE meeting and introduce me to nice people from the ALICE collaboration, with which I had enlightening discussions and insight into current research at ALICE. Working with him was a very nice experience, and he also showed personal interest besides the thesis, creating a pleasant environment.

I also want to thank Prof. Dr. Hansmann-Menzemer for agreeing to be the second referee for this thesis and agreeing to change the date of the colloquium on short term.

I especially want to thank Andrés Bórquez. He not only provided the code for the simulation setup, but also helped me learn important programming skills to set up the analysis. He took much time to solve problems with me and was always very cheerful and kind. We also had nice conversations beyond the topics of my thesis, making him not only a colleague, but a friend.

Overall, the ALICE group at the Institute was always really open-hearted and friendly, making working there more fun.

Thanks go out to my friends, that talked with me about stuff and have given me interesting ideas to pursue and solve problems with. They also helped to encourage me facing those problems.

Lastly, I want to thank my father for all the help and encouragement over the years and to give me the opportunity to study away from home. Without him, I would not be able to pursue my interests and dreams.

Erklärung

Ich versichere, dass ich diese Arbeit selbstständig verfasst und keine anderen als die angegebenen Quellen und Hilfsmittel benutzt habe.

Heidelberg, den 23.09.2024